



Algorithm Theoretical Basis Document (ATBD)  
for the  
Conical-Scanning Microwave Imager/Sounder (CMIS)  
Environmental Data Records (EDRs)

Volume 1: Overview  
Part 2: Spatial Data Processing

Covering: Footprint Matching and Interpolation  
Gridding  
Imagery EDR

**Version 1.2 – 15 March 2001**

**Solicitation No. F04701-01-R-0500**

Submitted by:  
**Atmospheric and Environmental Research, Inc.**  
**131 Hartwell Avenue**  
**Lexington, MA 02421-3126**

With contributions by:  
**John Galantowicz, Thomas Nehrkorn, Ross Hoffman, Alan Lipton**

Prepared for:  
**Boeing Satellite Systems**  
**919 Imperial Avenue**  
**El Segundo, CA 90245**



This page intentionally left blank.

## REVISION HISTORY

Version	Release Date	POC	Comments
1.0	11 Jan., 2001	Galantowicz	Initial partial draft release.
1.1	6 Feb., 2001 (PDR)	Galantowicz	Minor edits.
1.2	22 Feb., 2001	Galantowicz	Filled sections for imagery and gridding, added appendices C and D

## RELATED CMIS DOCUMENTATION

### Government Documents

Title	Version	Authorship	Date
CMIS SRD for NPOESS Spacecraft and Sensors	3.0	Associate Directorate for Acquisition NPOESS IPO	2 March 2001

### Boeing Satellite Systems Documents

Title		Covering
ATBD for the CMIS TDR/SDR Algorithms		
<b>ATBD for the CMIS EDRs</b>	<b>Volume 1: Overview</b>	Part 1: Integration <b>Part 2: Spatial Data Processing</b> <ul style="list-style-type: none"> <li>• Footprint Matching and Interpolation</li> <li>• Gridding</li> <li>• Imagery EDR</li> </ul>
	Volume 2: Core Physical Inversion Module	
	Volume 3: Water Vapor EDRs	Atmospheric Vertical Moisture Profile EDR Precipitable Water EDR
	Volume 4: Atmospheric Vertical Temperature Profile EDR	
	Volume 5: Precipitation Type and Rate EDR	
	Volume 6: Pressure Profile EDR	
	Volume 7: Cloud EDRs	Part 1: Cloud Ice Water Path EDR
		Part 2: Cloud Liquid Water EDR
		Part 3: Cloud Base Height EDR
	Volume 8: Total Water Content EDR	
	Volume 9: Soil Moisture EDR	
	Volume 10: Snow Cover/Depth EDR	
	Volume 11: Vegetation/Surface Type EDR	
	Volume 12: Ice EDRs	Sea Ice Age and Sea Ice Edge Motion EDR Fresh Water Ice EDR

Title		Covering
	Volume 13: Surface Temperature EDRs	Land Surface Temperature EDR Ice Surface Temperature EDR
	Volume 14: Ocean EDR Algorithm Suite	Sea Surface Temperature EDR Sea Surface Wind Speed/Direction EDR Surface Wind Stress EDR
	Volume 15: Test and Validation	All EDRs

**Bold** = this document

## TABLE OF CONTENTS FOR VOLUME 1, PART 2

<b>REVISION HISTORY.....</b>	<b>4</b>
<b>RELATED CMIS DOCUMENTATION .....</b>	<b>4</b>
<b>TABLE OF CONTENTS.....</b>	<b>6</b>
<b>LIST OF TABLES .....</b>	<b>8</b>
<b>LIST OF FIGURES .....</b>	<b>9</b>
<b>1. Introduction.....</b>	<b>10</b>
<b>2. Footprint matching.....</b>	<b>10</b>
2.1. Objectives and requirements .....	10
2.2. Historical and background perspective of proposed algorithm.....	12
2.3. Instrument characteristics and derived requirements .....	15
2.4. Algorithm description .....	18
2.5. Algorithm Performance.....	20
2.5.1. Center of scan performance.....	20
2.5.2. Quarter-scan performance .....	24
2.5.3. Performance at edge-of-scan for 816 km altitude .....	27
2.5.4. Performance at center-of-scan 850 km altitude.....	31
2.5.5. Constraints, limitations, and assumptions .....	32
<b>3. Gridding.....</b>	<b>32</b>
3.1. Background perspective of proposed algorithm.....	32
3.2. Algorithm description .....	34
3.3. Algorithm Performance.....	36
<b>4. Imagery EDR.....</b>	<b>36</b>
4.1. Objectives.....	36
4.2. SRD Requirements.....	37
4.3. Algorithm description .....	37
4.4. Algorithm Performance.....	38
<b>5. Glossary of Acronyms.....</b>	<b>39</b>
<b>6. References .....</b>	<b>40</b>
6.1. Technical Literature .....	40
<b>7. Appendix A — EFOV plots.....</b>	<b>42</b>
<b>8. Appendix B — Earth rotation.....</b>	<b>44</b>
<b>9. Appendix C — Errors due to the horizontal interpolation of EDRs .....</b>	<b>48</b>
9.1. Recursive Filter Methodology and Formulas.....	48
9.2. Error Budget Calculations.....	49
9.2.1. Methodology .....	49
9.2.2. Computational Details.....	49
9.2.3. Example Calculations.....	50
9.3. Results for all Cases and Times .....	54
9.4. Discussion/Conclusions .....	55
<b>10. Appendix D — Estimate of Cell Mismatch Errors .....</b>	<b>56</b>
10.1. Introduction .....	56
10.2. Convolution filters.....	56
10.3. High resolution model simulations and preprocessing .....	59
10.4. Definition of statistics .....	63
10.5. Example calculations.....	63
10.6. Results .....	70
10.6.1. All variables .....	70

10.6.2. Further RE statistics using masking for the hydrometeors.....	72
10.7. Discussion .....	73
10.8. Evaluation for Sea Surface Temperature .....	74
10.9. Acknowledgments.....	75

## LIST OF TABLES

Table 2-1: Instrument Characteristics (833 km altitude is default).....	16
Table 2-2: Footprint matching performance evaluated at center-of-scan .....	20
Table 2-3: Footprint matching performance evaluated at quarter-scan .....	25
Table 2-4: Footprint matching performance evaluated at edge-of-scan, 816 km altitude	28
Table 2-5: Footprint matching performance evaluated at center-of-scan, 850 km altitude	31
Table 4-1: SRD Requirements for the Imagery EDR .....	37
Table 4-2: Imagery EDR nominal performance.....	39
Table 4-3: Imagery EDR excluded conditions.....	39
Table 9-1: Statistics for Bonnie low-level mixing ratio (see text) .....	50
Table 9-2: Time-averaged RMS absolute aggregate and component error, all cases...	54
Table 9-3: Time-averaged RMS relative aggregate and component error, all cases .....	54



## LIST OF FIGURES

Figure 2-1: Top: A, B, C, and D scan arcs swept in one CMIS scan cycle. Bottom: Enlargements showing the relative geometry of a single A scan arc (solid line) to multiple C scan arcs (dashed). The C scan arcs are separated by 12.5 km along-track.....	17
Figure 2-2: Diagrams of composite footprint positioning patterns.....	18
Figure 2-3: COS 6H, 10H, and 89H composites for 50 km HCS, 833 km altitude.....	22
Figure 2-4: COS 18H composites for 25, 20, and 15 km HCS, 833 km altitude.....	23
Figure 2-5: COS 89H composites for 25, 20, and 15 km HCS, 833 km altitude.....	24
Figure 2-6: Quarter-scan 6H composite for 50 km HCS, 833 km altitude.....	26
Figure 2-7: Quarter-scan 18H and 89H composites for 25 km HCS, 833 km altitude....	27
Figure 2-8: EOS 6H and 18H composites for 50 km HCS, 816 km altitude.....	30
Figure 2-9: EOS 18H composites for 25 km HCS, 816 km altitude.....	30
Figure 2-10: EOS 10H composite for 40 km HCS, 816 km altitude.....	31
Figure 4-1: Overall CMIS processing flow including Imagery EDR.....	38
Figure 7-1: 6, 10, 18, and 36 GHz effective footprint patterns.....	42
Figure 7-2: 60, 89, 166, and 183 effective footprint patterns.....	43
Figure 7-3: EFOVs plotted at center-of-scan to show coincidence.....	44
Figure 9-1: The low-level mixing ratio field (kg/kg) for the Bonnie case at forecast hour 48. .....	52
Figure 9-2: The low-level mixing ratio field (kg/kg) for the Bonnie case at forecast hour 48, filtered with the SURF (true values, zs).....	52
Figure 9-3: The low-level mixing ratio field (kg/kg) for the Bonnie case at forecast hour 48, filtered with the TQGF (sensor values, zg).....	53
Figure 9-4: The low-level mixing ratio field (kg/kg) for the Bonnie case at forecast hour 48, filtered with the TQGF and recursive filter (interpolated values, zrf). ....	53

## 1. Introduction

The three CMIS tasks covered by this document—footprint matching, gridding, and imagery generation—deal with the spatial properties of sensor-sampled data, EDR inputs, and EDR products.

- Footprint matching is the process by which multiple sensor samples distributed horizontally on the earth's surface (or, more generally, on a surface defined at any height relative to a reference geoid) are used to produce a single composite sample at or near a particular location (interpolation) and with a particular spatial weighting pattern (pattern matching). For our purposes, the composite footprint location is always defined relative to the along-scan and along-track coordinate system of the sensor samples on the geoid. Typically, the objective of footprint matching for the retrieval of a given EDR is to create composite footprints with horizontal spatial resolution (HSR) equal to the EDR horizontal cell size (HCS) for each channel used in the EDR's derivation. Footprint matching performance, as considered here, is a function of the spatial weighting function (location and distribution) of the composite footprint without regard to the geophysical field sampled—that is, brightness temperature or the factors governing brightness temperature spatial properties including the retrieved EDRs.
- Gridding is the process by which one geophysical field is transformed from its sampled coordinates to another coordinate set. Examples include 1) regridding of slant-path atmospheric profile retrievals with altitude-dependent coordinates to the coordinates of the retrieval at a selected atmospheric layer (e.g., surface) and 2) regridding of satellite scan/track-coordinate retrievals to a fixed earth-grid (map) coordinate system. Our approach to regridding includes analysis of the expected spatial properties of the geophysical field sampled and the measurement's estimation errors and spatial properties.
- Imagery generation is a CMIS requirement through the imagery EDR. The content of the imagery EDR is brightness temperature data with properties consistent with the retrieval of the other EDRs and suitable for display. Imagery data at the CMIS sampled resolution is available through the SDR products (see *ATBD for CMIS TDR/SDR Algorithms*). Since most EDRs are retrieved based on composite footprint brightness temperatures, composite TBs will also be provided for each channel and composite footprint size combination used in the generation of the EDR. For example, the LST EDR's HCS is 50 km and channels at 10 GHz and up may be used in its derivation. The imagery product will therefore include ~50 km HSR composite footprint brightness temperatures at each of these channels sampled in the scan/track coordinate system—that is, the brightness temperatures will be located along the main conical arcs scanned by the sensor. The imagery product will also include brightness temperatures in the same fixed earth-grid (map) formats that are used to report some EDRs (e.g., soil moisture, snow cover, etc.)

The purpose of this document is to provide all the information necessary to understand, operate, further develop, and use the products of the CMIS spatial processing algorithms. Section 2 deals with footprint matching, section 3 with gridding, and section 4 with the imagery EDR. We described the relevant instrument characteristics and the algorithms' requirements, historical background, mathematical formulation, and predicted performance measures.

## 2. Footprint matching

### 2.1. Objectives and requirements

The objectives of footprint matching are to simultaneously 1) optimize the collocation of the horizontal weighting functions associated with the radiometric data of the various CMIS

channels and used in the derivation of the CMIS EDRs and 2) minimize the radiometric noise in the data. (Radiometric noise is reduced when noisy data from statistically independent sensor observations are averaged.) Although separate criteria for each of these objectives are easily devised—for example, match footprints such that their HSR is equal to an EDR's HCS or reduce radiometric noise to below the levels of other EDR error sources—simultaneous requirements cannot be set without considering the spatial statistics of the retrieved EDR and other factors governing the radiometric signal.

Consider a scene consisting of radiometric data perfectly representing the signal in HCS-square cells and nearly continuously sampled horizontally. The scene is smooth or homogeneous if it can be re-created—by some interpolation method—from data sampled with spacing somewhat greater than  $HCS/2$  (undersampling) or with HSR somewhat greater than HCS (smoothing). Similarly, the scene may be effectively smooth if the errors incurred through re-creating it from undersampled or smoothed data are negligible compared to other error sources (e.g., radiometric noise). If we also include the EDR retrieval process, then for our purposes the scene is effectively smooth if the errors incurred through re-creating the continuously-sampled EDR scene from undersampled or smoothed EDR retrievals are negligible compared to other EDR retrieval error sources. In other words, a smooth scene is one for which EDR retrieval at a given HCS is not sensitive within reasonable limits to radiometric spatial sampling characteristics.

Although the EDR retrieval performance impact of radiometric noise can be readily addressed for most EDRs, the impact of spatial sampling characteristics strongly depends on the smoothness of the scene relative to other EDR retrieval errors. For example, 50 km SST scenes are typically smooth except near coastlines, storms, and some thermal eddies; and although soil moisture spatial variability is high at 1 km or lower scales, the differences between 40 and 50 km HSR sampling is typically small except (importantly) in proximity to water bodies. (See the corresponding sea EDR and soil moisture EDR ATBDs for more details.) In contrast, 20 km snow cover scenes are highly heterogeneous near the snow-no snow line where most of snow cover's dynamic range is found.

The footprint matching process is governed by two general rules. Firstly, footprint matching does not normally sacrifice the composite footprint HSR in order to further reduce radiometric noise for the following reasons:

- Even EDRs that may be smooth at the corresponding HCS have instances (like those listed above) where the scene is heterogeneous and spatial sampling becomes a more critical part of the retrieval error budget. These are the very circumstances for which HCS is a defining measurement characteristic.
- Spatial sampling is already compromised from the HCS-square cell ideal due to the Gaussian-like spatial weighting function and the relatively large HSR of the sensor. As a standard, the goal of footprint matching is to create a composite footprint whose HSR matches the HCS of the corresponding EDR in both along- and across-scan dimensions. Even where this is done perfectly, only about 70% of the footprint weight falls in the square cell.

As discussed below, the exceptions to this rule are noise-critical sea EDRs for which retrieval performance can be significantly enhanced by minimizing radiometric noise while increasing the composite HSR. Secondly, footprint matching does not sacrifice radiometric noise for better HSR except where the impact on EDR retrieval of better HSR is likely to outweigh the increase in HSR. The only case falling under this exception is the enhancement of 6 GHz data (68 km native HSR) to 50 km HSR for soil moisture retrieval (40 km HCS). As discussed in the *ATBD*

for the CMIS Soil Moisture EDR (AER, 2000), 50 km-enhanced 6 GHz data improves soil moisture retrieval performance despite noise amplification and errors budgeted to the 40 vs. 50 km HSR difference.

## 2.2. Historical and background perspective of proposed algorithm

The basis for the CMIS footprint matching methodology is the so-called optimum interpolation formalism first applied to passive microwave data by Stogryn (1978) and adapted for SSM/I by Poe (1990). Optimum interpolation for passive microwave data is a special case of the more generalized geophysical measurement inversion methodology introduced by Backus and Gilbert (1970). As described below, the Backus-Gilbert theory provides a mechanism for trading-off spatial resolution and measurement noise. This feature is described by Stogryn (1978), and Farrar and Smith (1992) apply it to enhance the spatial resolution of SSM/I 19, 22, and 37 GHz data while controlling the inevitable noise amplification. Poe's (1990) solution intentionally puts the full weight on noise reduction and notes that image degradation has been observed as an additional bi-product of resolution enhancement techniques. In our approach, the trade-off mechanism is used sparingly for resolution enhancement (it is applied only for enhancing 68 km 6 GHz data to 50 km HSR) but is maintained throughout to insure that noise is optimized at the specified resolution.

The following material describes the basic process by which weighting coefficients  $a_i$  are derived for CMIS footprint matching. Application of the coefficients by the footprint matching algorithm transforms  $N$  neighboring directly measured sensor-footprint brightness temperatures  $T_{Bi}$  to composite-footprint brightness temperatures  $T_{Bc}$ . This process is summarized by the following equation:

$$T_{Bc} = \sum_{i=1}^N a_i T_{Bi} . \quad (1)$$

As this equation shows, the footprint matching algorithm itself is easily implemented. In contrast, derivation of the coefficients requires detailed knowledge of the instrument scan pattern and antenna patterns as well as specification of factors limiting  $N$ , the composite footprint locations relative to the scan pattern, and the composite footprint spatial weighting function, among other things. These details are left to the later discussion of algorithm implementation.

Following the notation of Stogryn (1978) and Poe (1990), let  $G(\rho_A, \rho)$  be the *effective* antenna gain for the earth coordinate location  $\rho$  when the gain pattern is centered at location  $\rho_A$  (defined further below). The effective antenna gain pattern is related to the *instantaneous* sensor pattern  $G_I$  by integrating over the sample integration time  $\tau$ :

$$G(\rho_A, \rho) = \frac{1}{\tau} \int_{-\tau/2}^{\tau/2} dt G_I(\hat{s}_0(t), \hat{s}(t)) \left[ \frac{-\hat{s}(t) \cdot \hat{\rho}}{s^2(t)} \right] \quad (2)$$

where  $\hat{s}_0(t)$  is the antenna bore-sight direction (sensor-to-earth) at time  $t$ ,  $\hat{s}(t)$  is the unit vector from the sensor to the (fixed) position  $\rho$ , and  $\hat{\rho}$  is the earth-normal vector at  $\rho$ . (The bracketed expression converts the differential solid angle of the instantaneous pattern to an earth surface differential area:  $d\Omega = [-\hat{s} \cdot \hat{\rho} / s^2(t)] dA$ .) The effective antenna pointing direction corresponding to  $\rho_A$  is given by:

$$\hat{s}_A = \frac{1}{\tau} \int_{-\tau/2}^{\tau/2} dt \hat{s}_0(t) \quad (3)$$

The  $i$ th measured brightness temperature is the gain-weighted integral of brightness temperature over the earth's surface:

$$T_{Bi}(\rho_{Ai}) = \int_E dA G(\rho_{Ai}, \rho) T_B(\rho). \quad (4)$$

(Note that where earth-surface integrals are indicated in practice the integral over a more reasonable area is taken. In either case,  $G$  must be normalized such that the integral of  $G$  over the area is equal to 1.)

(1) and (4) lead to the definition of the composite antenna gain function (or footprint):

$$G_c(\rho_r, \rho) = \sum_{i=1}^N a_i G(\rho_{Ai}, \rho). \quad (5)$$

Let  $G_r(\rho_r, \rho)$  be a reference footprint pattern which we would like the composite footprint to match when the reference is centered at  $\rho_c$ . (Note that  $\rho_r$  is *defined* for  $G_r$  but is an attribute assigned to  $G_c$ . A true bore-sight position for the composite  $G_c$  must be defined in terms of some objective measure of the beam center such as it's center of weight.) Then we would like to find a criterion which minimizes the error  $e$  in the estimate of  $T_{Br}(\rho_r)$ , the brightness temperature that would be measured by an instrument with footprint  $G_r(\rho_r, \rho)$ :

$$\begin{aligned} e &= |T_{Br}(\rho_r) - T_{Bc}(\rho_r)| \\ &= \left| \iint_E dA [G_r(\rho_r, \rho) - G_c(\rho_r, \rho)] T_B(\rho) \right|. \end{aligned} \quad (6)$$

In words, brightness temperature estimation error *due to spatial sampling* will be minimized when the  $a_i$  can be selected such that  $G_c$  closely matches  $G_r$ . As a first constraint, for  $G$  normalized as described above, a precise match is only possible if the sum of the  $a_i$  is 1. As a second constraint, Stogryn suggests the resolution cost function:

$$Q_R = \iint_E dA \left[ G_r(\rho_r, \rho) - \sum_{i=1}^N a_i G(\rho_{Ai}, \rho) \right]^2 J(\rho_r, \rho) \quad (7)$$

where  $J$  is a penalty function that may be used to produce some desirable footprint feature but is set to unity here. And a final constraint on the  $a_i$  will be used to minimize radiometric noise, as discussed below.

Let  $(\Delta T_i)^2$  be the sensor sample  $i$  measurement variance. Then from (1) the variance in  $T_{Bc}$  is given by:

$$(\Delta T_c)^2 = \mathbf{a}^T \mathbf{E} \mathbf{a} \quad (8)$$

where  $\mathbf{E}$  is the error covariance matrix of for the  $N$  measurements contributing to the composite. Because the same noisy calibration coefficients are applied to multiple samples, noise in some samples is correlated. Otherwise,  $\mathbf{E}$  would be a diagonal matrix and the composite variance would be due to sample-noise only:

$$(\Delta T_{cs})^2 = (\Delta T_{is})^2 \sum_{i=1}^N a_i^2 = (\Delta T_{is})^2 (NRF)^2 \quad (9)$$

where  $(\Delta T_{is})^2$  is the component of the sensor sample noise realized at the time of sampling and NRF is a "noise reduction factor" and is discussed further below. If we consider both sample-time and calibration noise, then the total composite measurement variance is:

$$(\Delta T_c)^2 = (\Delta T_{cs})^2 + (\Delta T_{cc})^2. \quad (10)$$

For CMIS, the calibration noise component of each measurement  $(\Delta T_{ic})^2$  is small compared to sample-time noise. To estimate  $(\Delta T_{cc})^2$ , we assume that the calibration coefficient set is applied one line at a time. (It may also be applied to multiple lines with somewhat more math.) Then the composite sample noise due to calibration is given approximately by:

$$(\Delta T_{cc})^2 = \frac{(\Delta T_{cal})^2}{k} \sum_{i_t=1}^{n_t} \left[ \sum_{i_s=1}^{n_s(i_t)} a(i_t, i_s) \right]^2 = \frac{(\Delta T_{cal})^2}{k} (CIF)^2 \quad (11)$$

where each calibration point consists of  $k$  calibration target observations with  $(\Delta T_{cal})^2$  effective measurement noise,  $n_t$  is the number of lines along-track contributing to the composite, and  $n_s$  is the number of samples along-scan.

Having defined expressions for composite footprint radiometric noise, we can now complete specification of a cost function to constrain the  $a_i$  solution that includes both the spatial function and noise. We chose to use consider only the sample-time noise component of the composite measurement noise which results in the following noise cost function:

$$Q_N = (\Delta T_{cs})^2 = (\Delta T_{is})^2 \sum_{i=1}^N a_i^2. \quad (12)$$

We combine (7) and (12) in a single cost function to allow control of the resolution-noise trade-off (after Stogryn, 1978, and Farrar and Smith, 1992):

$$Q = Q_R \cos \gamma + Q_N w \sin \gamma \quad (13)$$

where  $w$  can be used to insure dimensional and scale consistency between  $Q_R$  and  $Q_N$  (that is, brightness temperature variance units or similar) and  $0 \leq \gamma \leq \pi/2$  allows emphasis to be placed on resolution ( $\gamma$  close to 0) or noise error minimization.

With  $Q$  defined in this manner, the solution of the minimization problem (the vector of  $a_i$ ,  $\mathbf{a}$ ) is given by (Stogryn, 1978, following Backus and Gilbert, 1970):

$$\mathbf{a} = \mathbf{Z}^{-1} \left[ \cos \gamma \mathbf{v} + \frac{1 - \cos \gamma \mathbf{u}^T \mathbf{Z}^{-1} \mathbf{v}}{\mathbf{u}^T \mathbf{Z}^{-1} \mathbf{u}} \mathbf{u} \right] \quad (14)$$

where

$$\mathbf{Z} = \mathbf{G} \cos \gamma + \mathbf{I} w \sin \gamma, \quad (15)$$

$\mathbf{I}$  is the identity matrix, and  $w$  insures comparable resolution and noise cost scale as in (13).  $\mathbf{G}$  is the  $N \times N$  symmetric matrix whose elements represent the overlap between sampled footprints

$$\mathbf{G}_{ij} = \iint_E dA G_i(\rho) G_j(\rho). \quad (16)$$

The elements of vector  $\mathbf{u}$  give the total weight of each sensor footprint (identical to 1 due to normalization of  $G(\rho)$ )

$$u_i = \iint_E dA G_i(\rho). \quad (17)$$

And the elements of vector  $\mathbf{v}$  represent the overlap between each sampled pattern and the reference pattern:

$$v_i = \iint_E dA G_i(\rho) G_r(\rho). \quad (18)$$

Other details specific to the CMIS implementation of the footprint matching procedure are given in the algorithm description section below

### 2.3. Instrument characteristics and derived requirements

CMIS is a conically-scanning microwave radiometer with window channels—frequencies chosen to avoid atmospheric absorption lines—around 6, 10, 19, 37, and 88 GHz and atmospheric sounding channel families around 23, 50-60, 60, 166, and 183 GHz. The instrument rotates continuously at 31.6 rpm on an axis perpendicular to the ground taking observations along nearly semi-circular arcs centered on the satellite ground track. Successive arcs scanned by a single sensor channel are separated by about **12.5 km along-track** (depending on satellite altitude.) Calibration data is collected from a source (hot) and deep-space reflector (cold) viewed during the non-earth-viewing portion of the rotation cycle. Each observation (or sample) requires a finite sensor integration time which also transforms the sensor instantaneous field of view (IFOV)—the projection, or footprint, of the antenna gain pattern on the earth—into an observation effective field of view (EFOV). The start of each sample is separated by the sample time which is slightly longer than the integration time. The sample time is  $t_s = 1.2659$  ms for all channels with the exception of 10 GHz (exactly  $2t_s$ ) and 6.8 GHz ( $4t_s$ ). All samples fall on one of three main-reflector scan-arcs or a single secondary-reflector scan arc (166 and 183 GHz channels only).

Table 2-1 summaries CMIS design characteristics relevant to footprint matching for each sensor channel group. Multiple polarizations at the same frequency and sounding channel families around 50-60 and 183 GHz are listed as groups. Footprint 3dB EFOV and IFOV (effective and

instantaneous field-of-view) data were calculated at 833 km altitude, usually from the modeled H-pol. antenna patterns from each channel group. Exceptions are 23 GHz which we assume will be closely matched to the 18 GHz pattern, the 60H set which is represented by the 60HV pattern, and the 183 set which is represented by 183HA. The same modeled antenna patterns are used throughout the following analyses. Note that model patterns frozen in November, 2000 were used for the purposes of this analysis. Further changes to the design and fabrication margin are not included here. See section 2.5.5 for further discussion of these assumptions.

**Table 2-1: Instrument Characteristics (833 km altitude is default)**

	SELECTED SENSOR CHANNEL SPECIFICATIONS								
Channel prefix	6	10	18	23	36	60VL	89	166	183V
Channel suffixes	VH	VH, RL	VH, PM, RL	VH	VH, PM	A...V FFT	VH	V	ABC
Frequency range [GHz]	6.45- 6.8	10.6- 10.7	18.6- 18.8	23.6- 24.0	36.0- 37.0	50-60	87.0- 91.0	164.5- 167.5	173.4- 193.3
Cross-scan EFOV [km]	67.7	45.5	23.5	23.5	16.7	14.9	15.3	14.6	16.1
Along-scan EFOV [km]	39.3	24.8	15.5	15.5	10.3	8.2	8.1	8.8	9.0
Integration time [ms]	5	2.5	1.2	1.2	1.2	1.2	1.2	1.2	1.2
Along-scan sample spacing [km]	16.3	8.78	3.82	3.82	4.08	4.08	4.08	4.05	4.05
Cross-scan IFOV [km]	67.7	45.5	23.4	23.4	16.6	15.0	15.6	14.6	16.1
Along-scan IFOV [km]	37.8	24.2	15.3	15.3	9.9	7.7	7.8	8.4	8.7
Scan arc designation	A	B	C	C	A	A	A	D	D
Lookdown angle	46.98	48.70	45.40	45.40	47.00	47.01	46.99	46.85	46.86
Earth incidence angle	55.76	58.16	53.63	53.63	55.79	55.81	55.77	55.58	55.60
Field of regard [deg.]	127	113	145	145	127	127	127	129	129
833 km altitude swath width for sample centers [km]	1760	1754	1745	1745	1750	1751	1750	1751	1754
816 km altitude swath width for sample centers [km]	1719	1714	1707	1707	1710	1711	1709	1713	1714

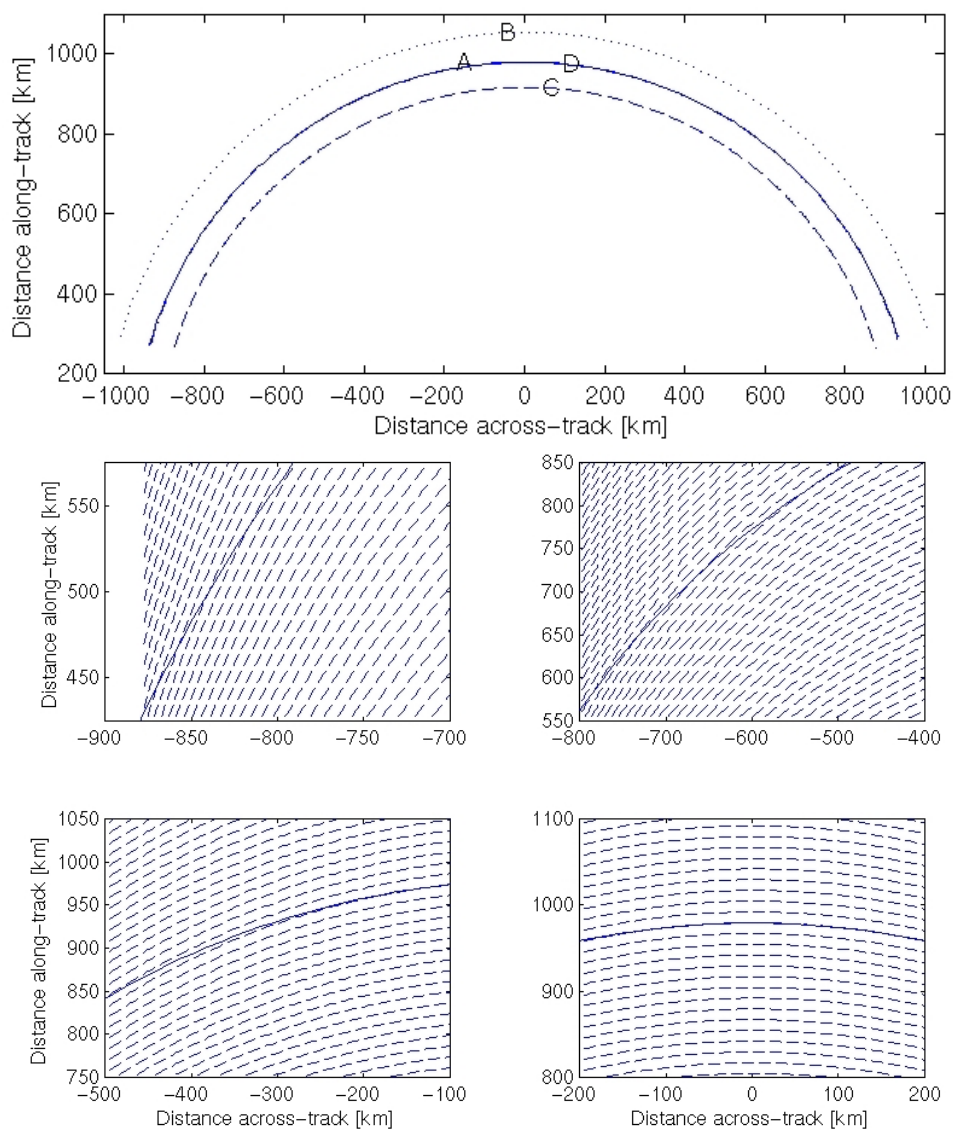
EFOV and IFOV are calculated here by projecting the footprint on the surface of a 6371 km sphere from the specified altitude and at the appropriate lookdown angle (sometimes called the zenith angle). EFOV pattern plots for these channels are given in Appendix A — EFOV plots. We define the FOV as the dimensions of the rectangle inscribing the 3dB contour of the footprint and having two sides parallel to and two sides perpendicular to the local scan arc tangent. The lookdown and earth incidence angles reported here are those required to collocate the 3dB center of weight of each footprint at the center of the scan arc. The 3dB center of weight is weighted-average position of points within the footprint 3dB contour and differs typically from the gain peak location which is the reference point for beam pointing.

Figure 2-1 summarizes CMIS scan geometry characteristics (without FOR limits). The top panel shows the four scan arcs on which all samples are centered projected on the surface of a 6371 km spherical earth from 833 km altitude. (For projections on the spherical earth presented here, the along-track distance is always measured out first then the across-track distance. That is, we walk 5 km along-track then 5 km across-track which does not put you in the same place as walking 5 km across-track then 5 km along-track.) Note that the A and D-arcs almost exactly overlap even though D-arc is scanned by the second high-frequency channel antenna reflector 180° after the



A-arc is scanned. The lower panels show enlargements of portions of the swath with a single A-arc overlaid on a series of C-arc from separate CMIS scans. All the scans are designed to meet at the center of scan COS (0 km across-track) by setting the COS along-track spacing of the A/B/C/D arcs from a single CMIS scan to be integer multiples of 12.5 km apart from each other. In the region 100-500 km off-center, the C-arcs diverge from the A-arc by about one scan increment. Beyond 500 km the divergence and cross-over frequency is increasingly more rapid. Note that the along-track spacing of the sensor samples (defined as the shortest distance from a point on one scan to the next scan) is largest at COS and decreases toward the edge of scan (EOS). We consider the channels with EFOV sizes less than 25 km to be undersampled (e.g., not Nyquist sampled) across-scan at COS. All channels are at least Nyquist sampled along-scan.

**Figure 2-1: Top: A, B, C, and D scan arcs swept in one CMIS scan cycle. Bottom: Enlargements showing the relative geometry of a single A scan arc (solid line) to multiple C scan arcs (dashed). The C scan arcs are separated by 12.5 km along-track.**



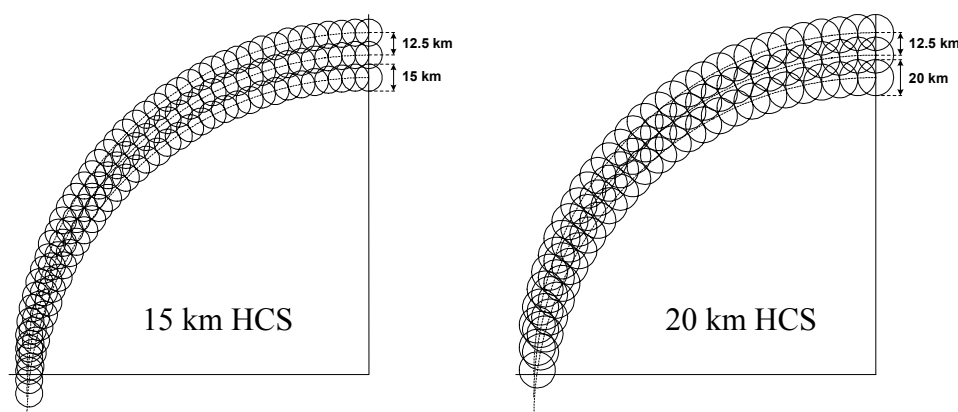
## 2.4. Algorithm description

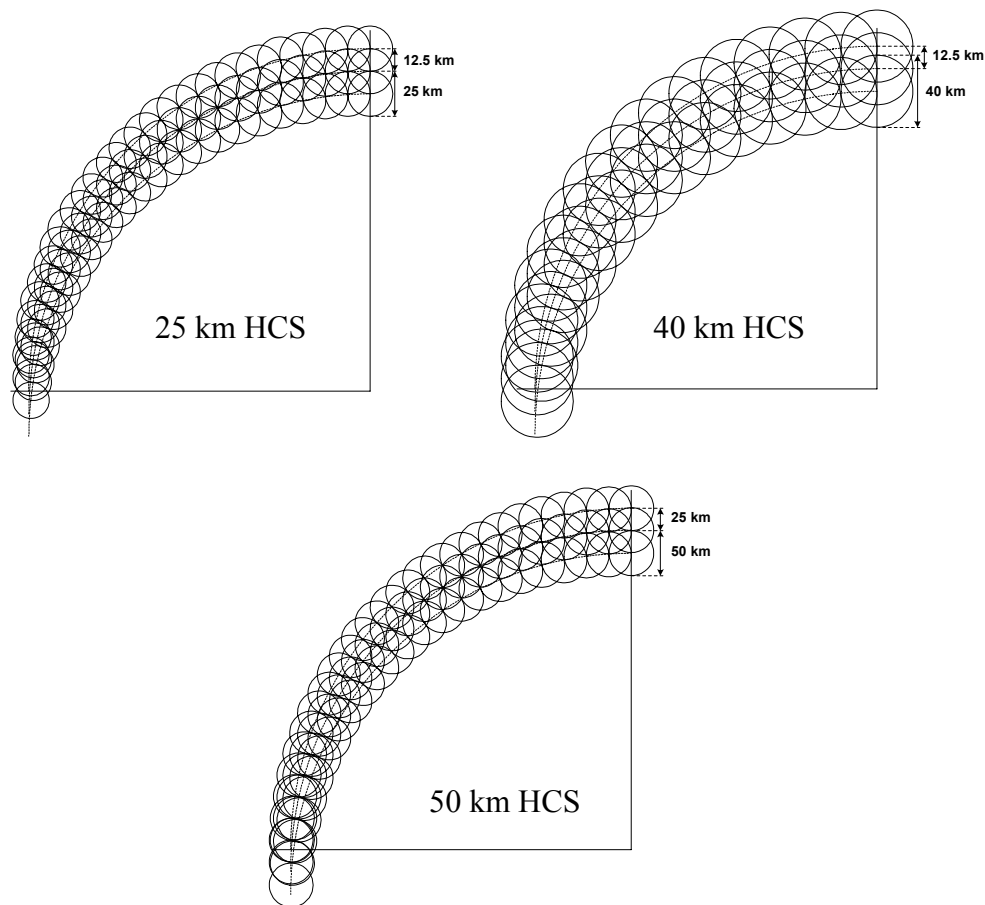
This section describes the design choices that govern the footprint matching procedure.

Footprint matching itself is accomplished through execution of (1).

- *Position the reference footprint in the scan-track coordinate system on a spherical earth.* When the scan-track coordinate system is used, the relative geometry of the sensor footprints and the reference is fixed. This allows us to compute weighting coefficients one time off-line either before launch or after launch if any scan pattern parameter has changed (e.g., satellite altitude). With the geometry fixed, calculation of a composite TB requires input of the channel and reference footprint size and position. With this information, the weighting coefficients and the corresponding sensor-sample locations can be extracted from a database and fed with the matching measured TBs through (1).
- *Position the reference footprints on or between the "A" scan arcs.* For retrievals that terminate in the scan-track reference frame of the sensor, this design has the advantage that no interpolation between scans is required at COS, where along-track sample spacing is worse, and between-track interpolation is never required for the under-sampled channels on the A-arc. Also, since the reference location and A-B-C-D scan geometry are always defined *relative* to the A-arc, footprint matching coefficients only need to be defined for a finite number of positions on the A-arc and at selected intervals between two A-arcs.
- *Define reference footprint positions to be oversampling.* For example, 25 km reference footprints are sampled with at most 12.5 km intervals. Figure 2-2 diagrams the nominal composite footprint positioning scheme for retrievals terminating in the scan-track coordinate system. For retrievals to be remapped to an earth grid, even more closely spaced sampling could be defined in order to control the resolution of the retrieval footprint. For example, the algorithm can determine footprint matching coefficients for reference footprints sampled at 1 km intervals along and between the A-arcs. Then for each satellite swath segment (a quarter orbit, for example) the algorithm identifies the reference positions closest to each of the earth-grid points within the swath. Composite TB calculation and geophysical retrievals are then performed only for the identified positions and the products are stored in the corresponding earth-grid location without further interpolation. This minimizes the number of retrievals that need to be performed and limits spatial errors to those under the control of the footprint matching process and the <1 km remapping error.

**Figure 2-2: Diagrams of composite footprint positioning patterns**





- *Choose the reference footprint HSR to be the EDR HCS (usually).* To be more precise, the reference footprint is (usually) the 89 GHz H-pol. footprint scaled such that its across-scan HSR equals the HCS and integrated along-scan until its along-scan HSR equals HCS. The exceptions include cases where 1) the sensor data is undersampled (18 GHz and up at COS) and 2) the HCS is 25 km or less. In these cases the across-scan reference HSR is currently set equal to the channel's HSR or the HCS, whichever is larger. The performance tables below always list the reference HSR size for each match.
- *Narrow down the number of possible contributing samples using the  $\mathbf{v}$  vector.* Initially, the number of samples considered for each composite includes at least 17 along-track and 13, 19, or 29 along-scan (depending on the sample spacing of the channel). The vector  $\mathbf{v}$  is calculated using (18) for each of these samples. Then the samples for which  $v_i$  is less than a given fraction (in the range 0.04-0.1) of  $\max(v_i)$  are discarded and the weighting coefficients  $a_i$  are calculated for the rest. It is undesirable to have too many samples contributing to a composite footprint because it increases the number of composites that a missing sample or scan line might affect.
- *Trade resolution for noise.* This is accomplished by choosing  $\gamma$  such that the composite HSR increases by less than a few percent from the optimum. In practice, we set  $\gamma = 0.75 \pi/2$  for most cases except 6 GHz matched to 50 km ( $\gamma = 0.0005 \pi/2$ ) and 10 GHz matched to 40 km (0.05). This step may in some cases reduce over-fitting to high-resolution features of the reference pattern and numerical instability in inverting  $\mathbf{Z}$  in (14).

## 2.5. Algorithm Performance

(See [EN #69](#) response for an evaluation of algorithm processing time.) Performance results are based on implementation and testing of the footprint matching algorithm at various locations along the A-arc. After calculating the weighting coefficients we use (5) to calculate the composite footprint gain function. The following metrics are used to evaluate the composite

- NRF: Noise reduction factor as given by (9)
- CIF: Calibration input factor as given by (11)
- CFOV: Composite footprint FOV across-scan and along-scan compared to RFOV, the reference footprint field of view
- N, N-track, N-scan: Number of samples, lines along-track, and positions along scan contributing to the composite
- Cell-weight: Total footprint weight in the HCS square cell. This is an integral similar to (17) but only integrated over the area of the square HCS cell specified. Note that cell-weight for a reference footprint with HSR = HCS is only about 70%.
- Coast-weight: Maximum footprint weight falling in a region beyond HCS/2 distance from the an edge of the HCS cell. This is the integral over a semi-infinite space separated from one edge of the cell by a distance HCS/2 and can be thought of as the weight falling across a coastline at that distance from the cell. The integral is calculated for regions above and below the cell in the across-scan direction and the maximum value is reported. Large values indicate that either the composite HSR is much larger than the HCS (which should be obvious) or that the composite has sidelobe-like spatial features. Coast-weight for a reference footprint with HSR = HCS is less than about 2%.

### 2.5.1. Center of scan performance

The following set of tables summarize footprint matching performance at center-of-scan for representatives of each channel group and at each EDR HCS. Altitude is 833 km. Note that the CFOV are always well matched to the RFOV along-scan (second component of FOV in table) because all sampling is designed to be Nyquist or better along-scan.

**Table 2-2: Footprint matching performance evaluated at center-of-scan**

50 km HCS	Channel designation															
	6H		10H		18H		36H		60HV		89H		166H		183HA	
RFOV [km]	50.2	50.4	50.2	50.4	50.2	50.4	50.2	50.4	50.2	50.4	50.2	50.4	50.2	50.4	50.2	50.4
CFOV [km]	50.7	49.2	51.2	50.7	50.2	50.9	50.3	51.1	50.2	51.3	48.2	51.1	50.4	51.1	50.4	51.3
Cell-weight [%]	68		66.5		68.9		69.2		70.2		70.4		69.6		70	
Coast-wt. [%]	5.4		2		0.2		0.2		0		0		0.1		0.1	
NRF	1.991		0.236		0.117		0.116		0.115		0.116		0.115		0.115	
CIF	3.003		0.595		0.465		0.45		0.445		0.444		0.447		0.446	
N	82		75		141		101		96		95		98		97	
N-track, N-scan	13	7	9	11	7	23	7	19	7	17	7	17	7	18	7	18

40 km HCS	Channel designation															
	6H		10H		18H		36H		60HV		89H		166H		183HA	
RFOV [km]	49.8	40.4	40.1	40.3	40.1	40.3	40.1	40.3	40.1	40.3	40.1	40.3	40.1	40.3	40.1	40.3
CFOV [km]	50.9	39.6	39.8	40.3	39.9	40.7	39.5	40.7	40.0	41.0	40.2	40.6	38.7	40.6	40.0	40.8
Cell-weight [%]	55.3		68.1		68.8		68.9		69.4		69.6		68.9		68.9	
Coast-wt. [%]	7.6		3.5		0.5		0.3		0		0		0.2		0.1	
NRF	2.505		0.517		0.156		0.148		0.144		0.143		0.144		0.142	
CIF	3.339		1.07		0.545		0.515		0.499		0.497		0.503		0.501	
N	76		72		99		88		63		63		65		76	
N-track, N-scan	13	7	10	9	7	18	7	17	5	15	5	15	5	15	5	17

25 km HCS	Channel designation															
	6H		10H		18H		36H		60HV		89H		166H		183HA	
RFOV [km]	--	--	33.4	25.3	25.1	25.2	25.1	25.2	25.1	25.2	25.1	25.2	25.1	25.2	25.1	25.2
CFOV [km]	--	--	34.5	25.6	25.1	25.1	23.9	25.5	22.1	25.4	21.6	25.3	23.5	25.5	22.4	25.4
Cell-weight [%]	--		52		67.4		67.8		66		65.8		67.2		66.3	
Coast-wt. [%]	--		10.3		2.7		2.3		0.4		0.1		1.9		0.6	
NRF	--		2.94		0.354		0.28		0.24		0.234		0.256		0.244	
CIF	--		3.587		0.912		0.733		0.649		0.637		0.686		0.66	
N	--		54		47		39		29		29		36		29	
N-track, N-scan	--	--	9	8	5	12	5	11	3	11	3	11	5	11	3	11

20 km HCS	Channel designation															
	6H		10H		18H		36H		60HV		89H		166H		183HA	
RFOV [km]	--	--	--	--	23.9	20.4	20.1	20.2	20.1	20.2	20.1	20.2	20.1	20.2	20.1	20.2
CFOV [km]	--	--	--	--	24.3	20.6	18.0	20.2	17.1	20.4	17.0	20.3	16.8	20.2	17.5	20.3
Cell-weight [%]	--		--		57.5		66.9		66.4		66.3		66.4		67	
Coast-wt. [%]	--		--		5.4		2.4		2.3		2.1		2.5		2.4	
NRF	--		--		0.44		0.418		0.328		0.311		0.357		0.34	
CIF	--		--		1.002		0.947		0.776		0.742		0.829		0.805	
N	--		--		41		25		23		23		23		23	
N-track, N-scan	--	--	--	--	5	11	3	9	3	9	3	9	3	9	3	9

15 km HCS	Channel designation															
	6H		10H		18H		36H		60HV		89H		166H		183HA	
RFOV [km]	--	--	--	--	23.8	16.0	17.1	15.2	15.4	15.5	15.9	15.5	15.0	15.1	16.5	15.5
CFOV [km]	--	--	--	--	24.2	17.2	16.5	15.3	14.8	15.3	14.9	15.2	14.5	15.0	15.7	15.3
Cell-weight [%]	--		--		43		60.4		65.7		64.6		67.6		62.3	
Coast-wt. [%]	--		--		14		4.6		1.6		3.1		2		2.3	
NRF	--		--		0.573		0.601		0.498		0.449		0.576		0.489	
CIF	--		--		1.055		1.145		0.985		0.906		1.1		0.978	
N	--		--		37		19		17		17		17		18	
N-track, N-scan	--	--	--	--	5	10	3	7	3	7	3	7	3	7	3	7

The following figures show composite and reference footprint contour plots for selected channels and HCS. The +s mark the positions of the sensor samples contributing to the calculation of the composite. The reference footprint is positioned at the plot axes origin.

- Figure 2-3 shows the differences between footprint matching results when the sensor footprint HSR is greater than, just less than, and much less than the reference HSR. Enhancement of the 67 km 6H footprint to 50 km creates large sidelobe features in the composite compared to 10H and 89H composites. We can use the coast-weight metric in the tables above to judge this quantitatively: 6H coast-weight is 5.4%, 10H is 2%, and 89H is 0%. Additional samples can potentially improve coast-weight performance but with diminishing value per sample farther from the footprint center. 6H is the best candidate for HSR enhancement because it is highly oversampled so more samples are available to keep the NRF (relatively) low.
- Figure 2-4 shows how the 23.5 km 18H footprint is matched at 25, 20, and 15 km HCS. In each case the along-scan composite HSR is close to the HCS while the across-scan HSR is at least 23.5 km. Since 18H is undersampled along-track at COS, accurate HSR enhancement is not possible. Similarly, footprint matching is imperfect where 18H is interpolated between scans as shown in the next section. Note that 18 and 23 channels are the only ones that are both undersampled and subject to interpolation to match footprints on the A-scan arc.
- Figure 2-5 shows composite footprints for the 15.3 km HSR 89H channel matched at 25, 20, and 15 km. Here the HSR problem mirrors that at 18H. 18H is undersampled along-track so the composite HSR are intentionally less than the 25 and 20 km HCS. The

alternative—that is, design composites to be greater than the HCS—was rejected because, as shown in the tables above, the cell-weight is much better (higher) when the footprint is less than the HCS. As with 18H, the composite matches the reference well along-scan.

**Figure 2-3: COS 6H, 10H, and 89H composites for 50 km HCS, 833 km altitude**

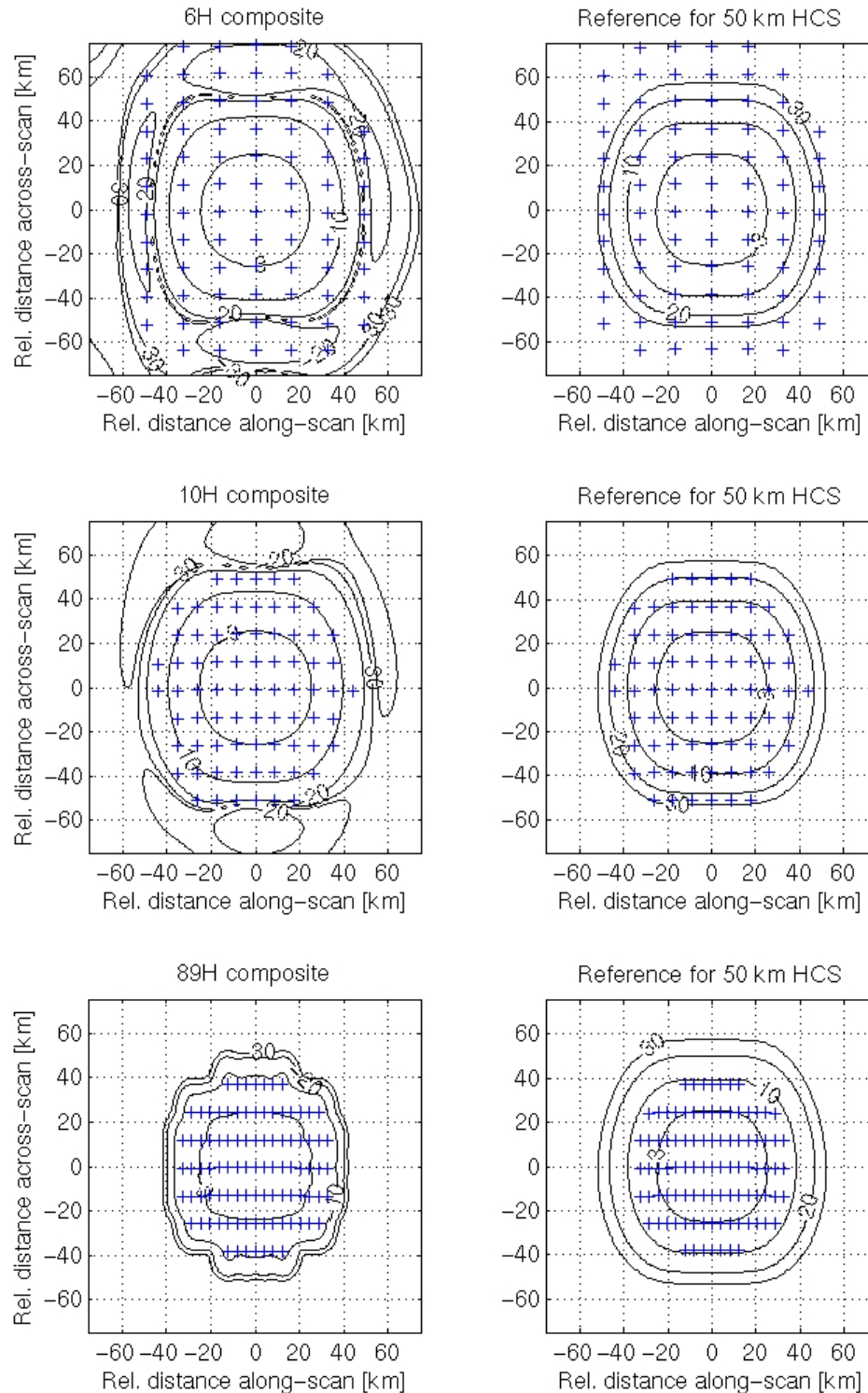


**Figure 2-4: COS 18H composites for 25, 20, and 15 km HCS, 833 km altitude**

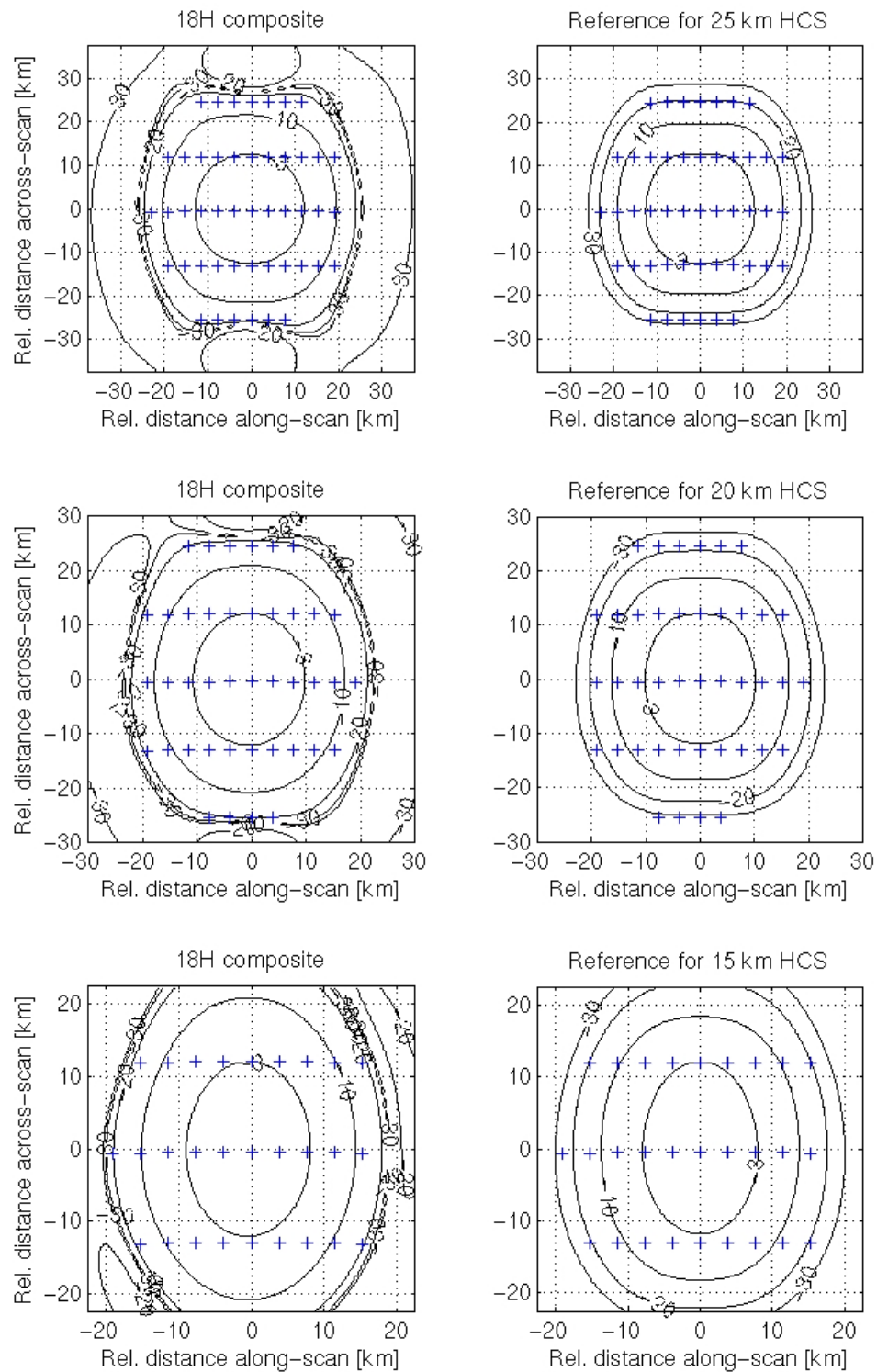
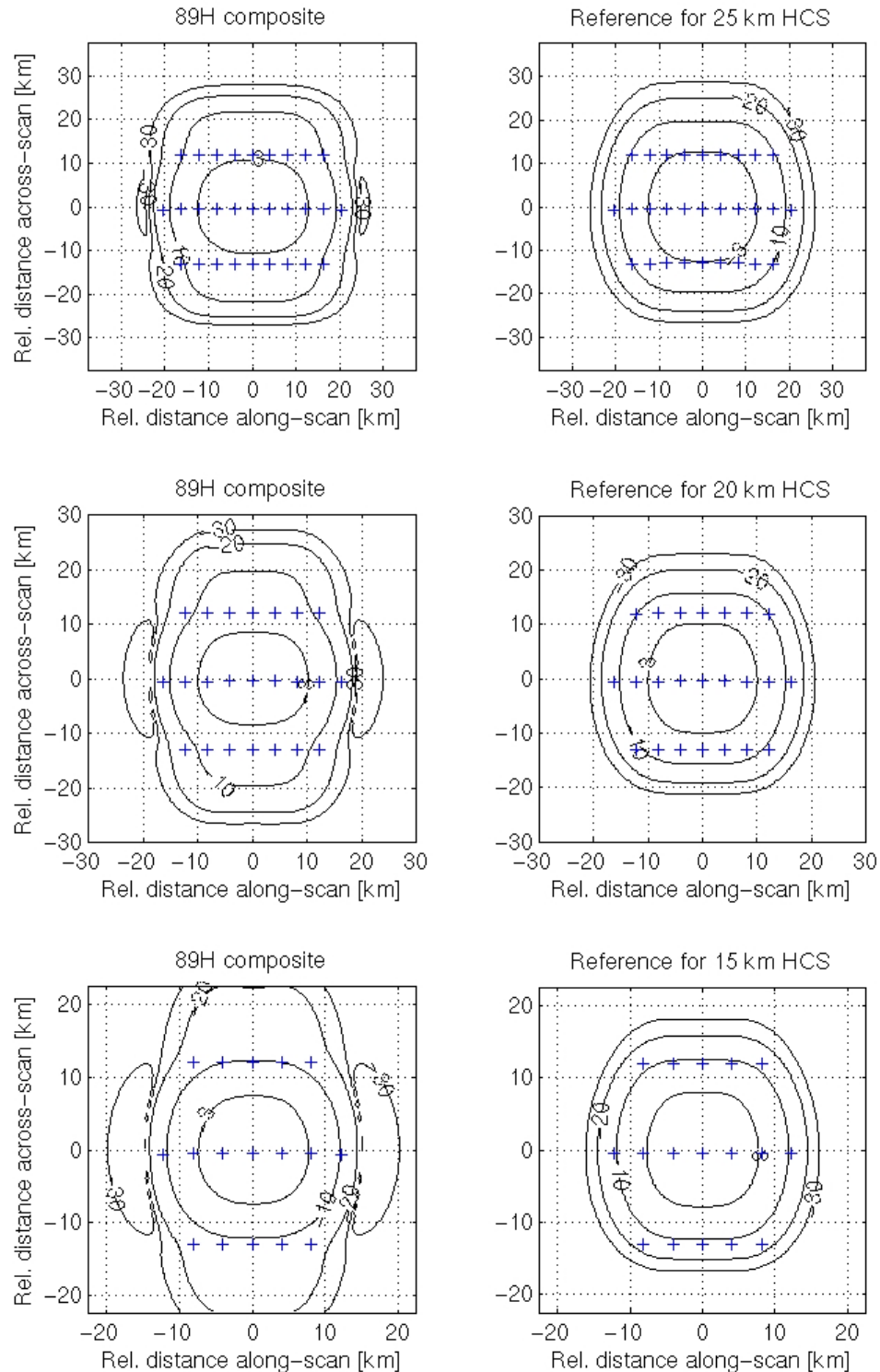




**Figure 2-5: COS 89H composites for 25, 20, and 15 km HCS, 833 km altitude**



### 2.5.2. Quarter-scan performance

The following set of tables summarize footprint matching performance at the quarter-scan location (415 km across-track from the satellite ground-track line) for representatives of each channel group and at each EDR HCS. Satellite altitude is 833 km.



**Table 2-3: Footprint matching performance evaluated at quarter-scan**

50 km HCS	Channel designation															
	6H		10H		18H		36H		60HV		89H		166H		183HA	
RFOV [km]	50.2	50.4	50.2	50.4	50.2	50.4	50.2	50.4	50.2	50.4	50.2	50.4	50.2	50.4	50.2	50.4
CFOV [km]	51.4	49.8	51.0	50.7	50.1	50.9	50.3	51.0	50.5	51.2	48.7	51.1	50.4	51.2	50.5	51.4
Cell-weight [%]	67.7		66.5		68.8		69.1		69.8		69.8		69.4		69.7	
Coast-wt. [%]	6.3		2		0.1		0.1		0		0		0.1		0	
NRF	1.443		0.227		0.11		0.11		0.109		0.109		0.109		0.109	
CIF	2.465		0.574		0.439		0.428		0.422		0.421		0.424		0.423	
N	93		84		157		110		106		106		110		107	
N-track, N-scan	15	10	10	12	8	27	7	21	7	21	7	21	7	21	7	21

40 km HCS	Channel designation															
	6H		10H		18H		36H		60HV		89H		166H		183HA	
RFOV [km]	49.8	40.4	40.1	40.3	40.1	40.3	40.1	40.3	40.1	40.3	40.1	40.3	40.1	40.3	40.1	40.3
CFOV [km]	52.3	39.9	39.8	40.4	40.0	40.7	39.9	40.7	40.4	40.9	40.2	40.8	39.7	40.6	40.4	40.8
Cell-weight [%]	54.7		68		68.8		68.8		69.4		69.8		69		68.9	
Coast-wt. [%]	9.8		2.7		0.3		0.1		0		0		0.1		0.1	
NRF	1.693		0.529		0.147		0.141		0.137		0.137		0.138		0.136	
CIF	2.72		1.113		0.516		0.491		0.479		0.477		0.482		0.478	
N	66		65		109		97		67		67		66		94	
N-track, N-scan	13	8	9	10	7	22	7	20	5	17	5	17	5	17	7	19

25 km HCS	Channel designation															
	6H		10H		18H		36H		60HV		89H		166H		183HA	
RFOV [km]	--	--	33.4	25.3	25.1	25.2	25.1	25.2	25.1	25.2	25.1	25.2	25.1	25.2	25.1	25.2
CFOV [km]	--	--	35.4	25.8	25.2	25.1	24.6	25.4	24.5	25.5	24.2	25.5	24.6	25.5	24.5	25.5
Cell-weight [%]	--		51.2		67.6		68.2		68.1		67.9		68.2		68.4	
Coast-wt. [%]	--		12.9		1.8		1.7		1		0.8		1.2		1.2	
NRF	--		1.556		0.336		0.267		0.235		0.229		0.246		0.238	
CIF	--		2.328		0.855		0.701		0.64		0.627		0.661		0.65	
N	--		49		51		45		40		39		42		41	
N-track, N-scan	--	--	9	8	5	15	5	13	5	12	5	12	5	13	5	12

20 km HCS	Channel designation															
	6H		10H		18H		36H		60HV		89H		166H		183HA	
RFOV [km]	--	--	--	--	23.9	20.4	20.1	20.2	20.1	20.2	20.1	20.2	20.1	20.2	20.1	20.2
CFOV [km]	--	--	--	--	24.5	20.5	19.0	20.3	17.7	20.3	17.7	20.3	17.5	20.2	18.1	20.3
Cell-weight [%]	--		--		57.7		67.4		66.6		66.6		66.5		66.9	
Coast-wt. [%]	--		--		4.6		2.8		1.7		1.3		2.1		1.8	
NRF	--		--		0.415		0.403		0.317		0.3		0.346		0.33	
CIF	--		--		0.928		0.917		0.752		0.718		0.806		0.783	
N	--		--		45		27		24		23		25		23	
N-track, N-scan	--	--	--	--	5	13	5	11	3	10	3	9	3	11	3	10

15 km HCS	Channel designation															
	6H		10H		18H		36H		60HV		89H		166H		183HA	
RFOV [km]	--	--	--	--	23.8	16.0	17.1	15.2	15.4	15.5	15.9	15.5	15.0	15.1	16.5	15.5
CFOV [km]	--	--	--	--	24.5	17.0	16.5	15.3	14.9	15.3	15.1	15.2	14.5	15.0	15.8	15.2
Cell-weight [%]	--		--		43.1		60.2		65.4		64.4		67.3		61.9	
Coast-wt. [%]	--		--		13.2		4.4		1.7		2.8		2.9		2.7	
NRF	--		--		0.542		0.604		0.494		0.443		0.576		0.487	
CIF	--		--		0.967		1.158		0.981		0.893		1.108		0.973	
N	--		--		41		19		17		17		19		17	
N-track, N-scan	--	--	--	--	5	13	3	9	3	7	3	7	3	9	3	8

The following figures show composite and reference footprint contour plots for selected channels and HCS. The +s mark the positions of the sensor samples contributing to the calculation of the composite. The reference footprint is positioned at the plot axes origin.

- Figure 2-6 shows enhancement of the 67 km HSR 6H footprint to 50 km. The composite match to the reference is similar to that at COS, with some sidelobe features. Note that the NRF has improved from 2.0 to 1.4 due to the additional samples with significant weight. (Additional samples don't improve NRF if their weighting coefficients are close to zero.)
- Figure 2-7 shows the composite footprints for 18H and 89H channels matched at 25 km. The higher effective sampling rate helps the 89H footprint match the 25 km reference better here than at COS. The composite HSR is now 24.2 km compared to 21.6 km at COS. The 18H composites have essentially the same shape as at COS although the NRF have improve somewhat with the additional weighted samples.

**Figure 2-6: Quarter-scan 6H composite for 50 km HCS, 833 km altitude**

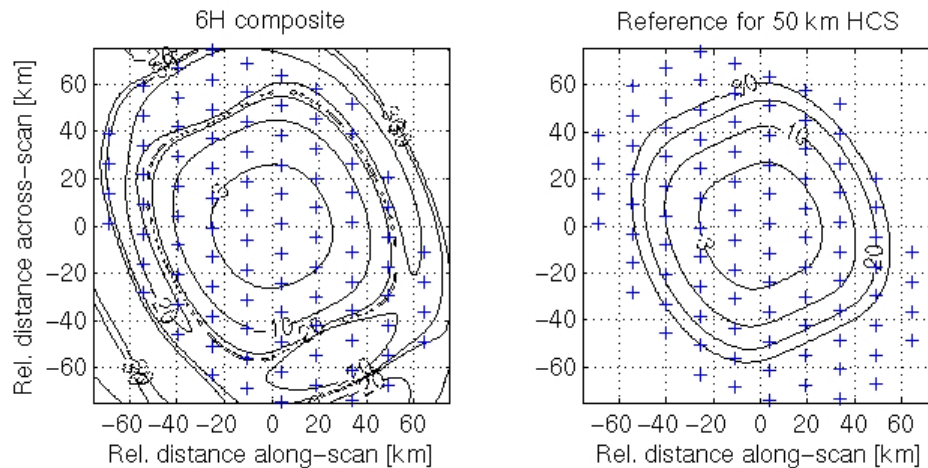
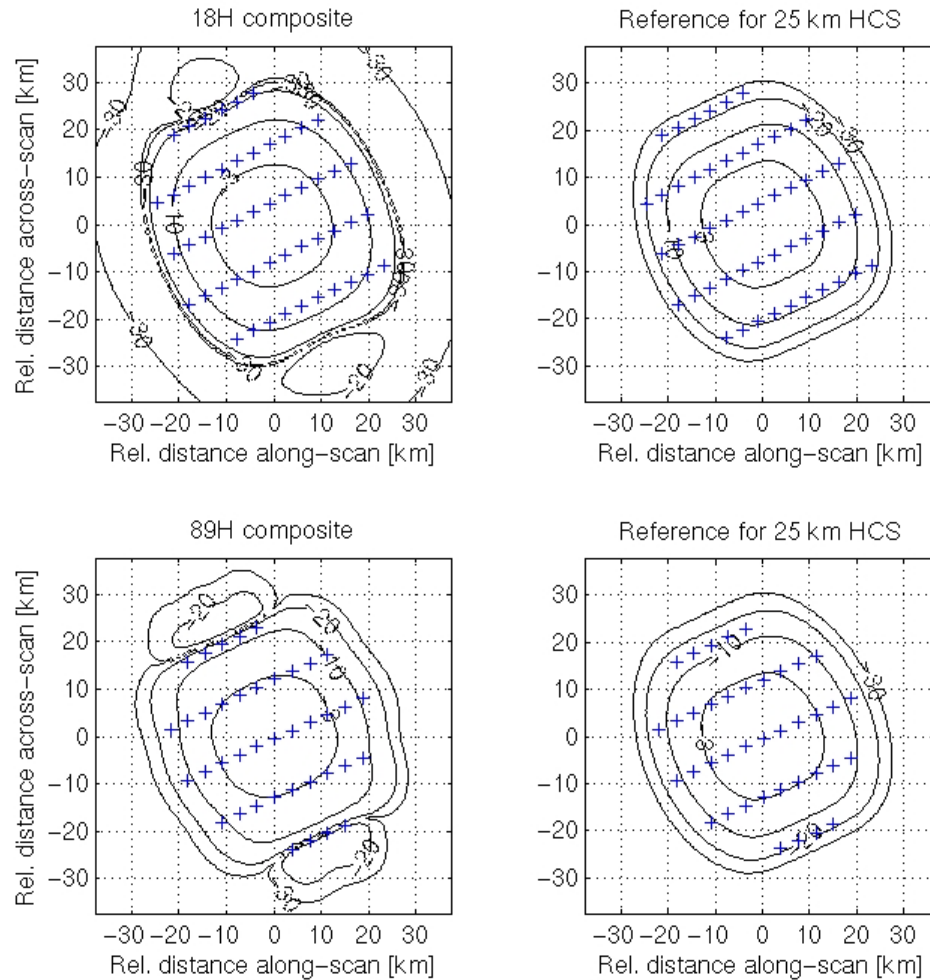


**Figure 2-7: Quarter-scan 18H and 89H composites for 25 km HCS, 833 km altitude**



### 2.5.3. Performance at edge-of-scan for 816 km altitude

The following set of tables summarize footprint matching performance at the edge-of-scan (EOS) and 816 km altitude. The EOS scan-arc position is different for each HCS. The across-track position of the reference point for each HCS is chosen to be HCS/2 distance or less from the edge of a 1700 km swath. That is, a circle of size HCS placed at the reference position would be inside the CMIS swath and its edge would just touch the edge of the swath. The field-of-regard specification (summarized in Table 2-1) governs the beginning and end sample for each channel and is intended to satisfy the 1700 km EDR swath width requirement even for low altitude CMIS operation. We show 816 km altitude test results here to demonstrate that the FOR is sufficient at each channel to meet EDR swath width requirements under the most stressing conditions. Note that some reference footprint HSR differ from the HCS because the footprint scaling method used to create reference footprints was tuned at 833 km altitude.

**Table 2-4: Footprint matching performance evaluated at edge-of-scan, 816 km altitude**

50 km HCS	Channel designation															
	6H		10H		18H		36H		60HV		89H		166H		183HA	
RFOV [km]	48.8	50.4	48.8	50.4	48.8	50.4	48.8	50.4	48.8	50.4	48.8	50.4	48.8	50.4	48.8	50.4
CFOV [km]	50.3	50.0	48.3	50.5	48.7	50.7	49.3	51.1	49.6	51.8	49.4	52.0	49.0	51.3	49.0	51.5
Cell-weight [%]	69.1		68.3		70.6		70.9		71.6		71.9		71.1		71.3	
Coast-wt. [%]	6.4		1.6		0.1		0.1		0		0		0		0	
NRF	1.401		0.191		0.076		0.086		0.088		0.088		0.085		0.084	
CIF	2.242		0.478		0.295		0.325		0.322		0.322		0.319		0.318	
N	117		109		295		174		171		171		183		183	
N-track, N-scan	21	14	15	17	17	46	12	35	12	34	12	34	13	36	12	36

40 km HCS	Channel designation															
	6H		10H		18H		36H		60HV		89H		166H		183HA	
RFOV [km]	48.4	40.3	39.0	40.3	39.0	40.3	39.0	40.3	39.0	40.3	39.0	40.3	39.0	40.3	39.0	40.3
CFOV [km]	51.0	39.5	38.6	40.4	38.8	40.6	39.0	40.7	39.2	41.0	39.4	41.1	39.2	40.7	39.1	40.8
Cell-weight [%]	56.2		69.5		70.4		70.4		70.9		71.1		70.5		70.5	
Coast-wt. [%]	9.4		2.8		0.2		0.1		0		0		0.1		0.1	
NRF	1.564		0.439		0.097		0.106		0.105		0.104		0.103		0.101	
CIF	2.33		0.908		0.339		0.369		0.359		0.357		0.358		0.356	
N	105		101		218		148		117		117		124		155	
N-track, N-scan	21	13	14	16	16	43	11	32	10	29	10	29	10	31	12	33

25 km HCS	Channel designation															
	6H		10H		18H		36H		60HV		89H		166H		183HA	
RFOV [km]	--	--	32.4	25.1	24.4	25.2	24.4	25.2	24.4	25.2	24.4	25.2	24.4	25.2	24.4	25.2
CFOV [km]	--	--	34.8	25.5	23.9	25.1	24.1	25.4	24.3	25.4	24.2	25.4	24.3	25.4	24.2	25.4
Cell-weight [%]	--		52.5		69.5		70		70.1		70.3		70.1		70.3	
Coast-wt. [%]	--		13.3		1.3		0.6		0.1		0		0.5		0.3	
NRF	--		1.407		0.229		0.203		0.175		0.17		0.181		0.176	
CIF	--		2.153		0.572		0.528		0.478		0.467		0.49		0.481	
N	--		72		98		69		62		62		70		71	
N-track, N-scan	--	--	13	13	11	27	9	22	7	21	7	21	8	23	8	23

20 km HCS	Channel designation															
	6H		10H		18H		36H		60HV		89H		166H		183HA	
RFOV [km]	--	--	--	--	23.2	20.4	19.5	20.2	19.5	20.2	19.5	20.2	19.5	20.2	19.5	20.2
CFOV [km]	--	--	--	--	23.0	20.3	19.1	20.2	19.1	20.4	19.0	20.3	19.2	20.3	19.1	20.3
Cell-weight [%]	--		--		59.8		69.6		69.8		70		69.8		70	
Coast-wt. [%]	--		--		3.3		1.4		0.8		0.5		1		0.9	
NRF	--		--		0.291		0.309		0.241		0.23		0.257		0.243	
CIF	--		--		0.646		0.691		0.576		0.557		0.604		0.581	
N	--		--		80		49		45		43		47		46	
N-track, N-scan	--	--	--	--	10	24	7	19	7	18	7	17	7	19	7	19

15 km HCS	Channel designation															
	6H		10H		18H		36H		60HV		89H		166H		183HA	
RFOV [km]	--	--	--	--	23.1	15.8	16.6	15.2	15.0	15.4	15.4	15.5	14.6	15.1	16.0	15.5
CFOV [km]	--	--	--	--	23.0	16.4	16.7	15.1	15.0	15.2	15.1	15.2	14.7	15.1	15.9	15.2
Cell-weight [%]	--		--		45.4		62.1		67.1		66.2		69		63.8	
Coast-wt. [%]	--		--		10.8		3.3		1.9		1.1		2.3		2	
NRF	--		--		0.393		0.493		0.4		0.348		0.483		0.379	
CIF	--		--		0.694		0.938		0.803		0.709		0.951		0.77	
N	--		--		67		35		28		26		33		33	
N-track, N-scan	--	--	--	--	10	23	6	17	5	14	5	14	6	16	6	17

The following figures show composite and reference footprint contour plots for selected channels and HCS. The +s mark the positions of the sensor samples contributing to the calculation of the composite. The reference footprint is positioned at the plot axes origin. In each case, the FOR truncates the samples at or beyond the edge of the 3dB contour of the reference footprint. For

example, the 50 and 25 km 3dB footprint contours each graze the last (left-most) column of 18H samples. Note that the higher EOS sampling rate helps keep the NRFs low despite the limit FOR places on the number of contributing samples.

**Figure 2-8: EOS 6H and 18H composites for 50 km HCS, 816 km altitude**

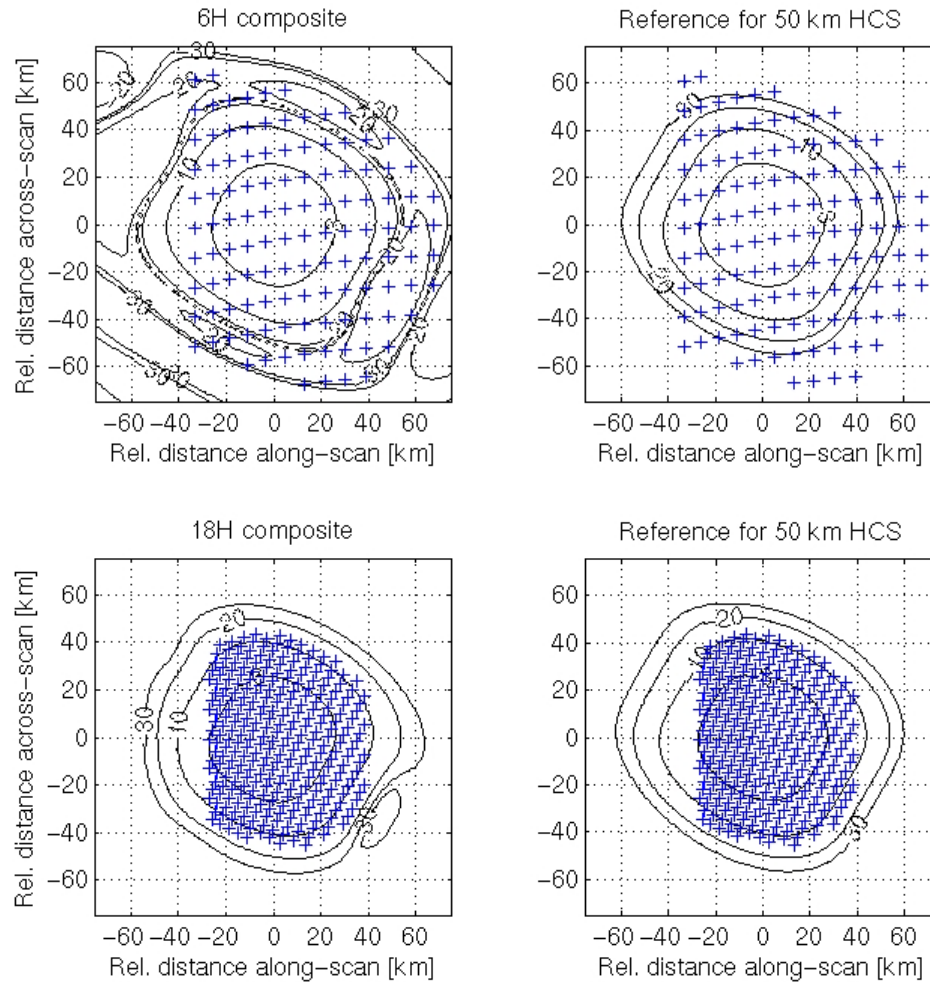


**Figure 2-9: EOS 18H composites for 25 km HCS, 816 km altitude**

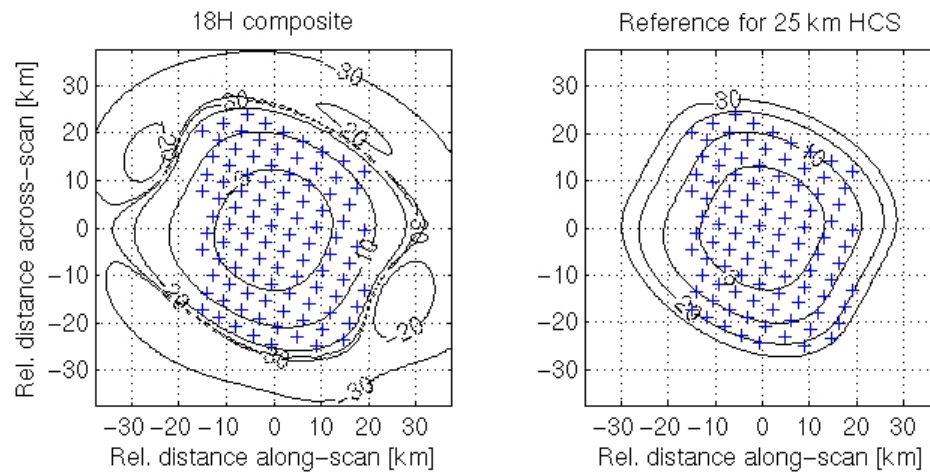
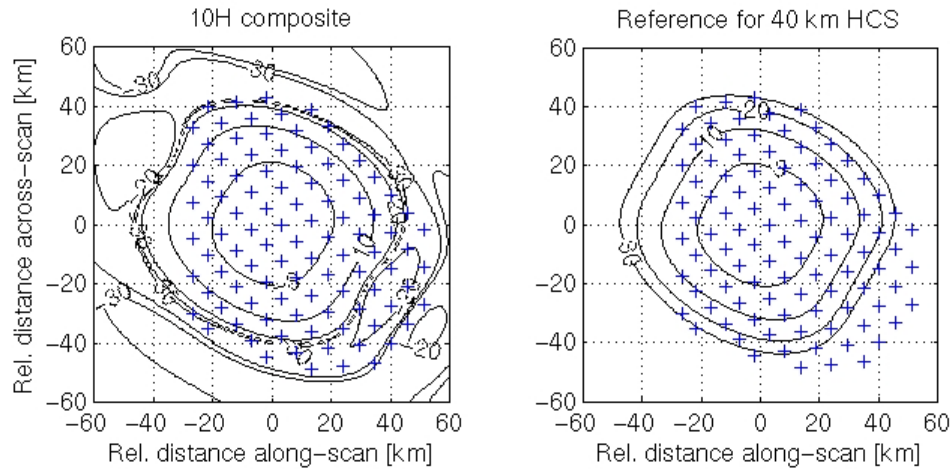


**Figure 2-10: EOS 10H composite for 40 km HCS, 816 km altitude**



#### 2.5.4. Performance at center-of-scan 850 km altitude

Sensor spatial resolution degrades as a function of higher satellite altitude. Below we show performance at 850 km using the same coefficient sets used at 833 km above. The intent is to show how the spatial characteristics of the composite footprint degrade gracefully with higher satellite altitude when noise performance (NRF) is held harmless.

**Table 2-5: Footprint matching performance evaluated at center-of-scan, 850 km altitude**

50 km HCS	Channel designation															
	6H		10H		18H		36H		60HV		89H		166H		183HA	
RFOV [km]	51.6	50.5	51.6	50.5	51.6	50.5	51.6	50.5	51.6	50.5	51.6	50.5	51.6	50.5	51.6	50.5
CFOV [km]	52.7	49.6	52.1	50.8	50.3	50.9	50.4	51.0	50.2	51.3	48.2	51.1	50.5	51.1	50.5	51.2
Cell-weight [%]	65.1		65.3		68.5		69		70.1		70.4		69.5		69.9	
Coast-wt. [%]	4.5		2		0.2		0.2		0		0		0.1		0.1	
NRF	1.991		0.236		0.117		0.116		0.115		0.116		0.115		0.115	
CIF	3.003		0.595		0.465		0.45		0.445		0.444		0.447		0.446	
N	82		75		141		101		96		95		98		97	
N-track, N-scan	13	7	9	11	7	23	7	19	7	17	7	17	7	18	7	18

40 km HCS	Channel designation															
	6H		10H		18H		36H		60HV		89H		166H		183HA	
RFOV [km]	51.3	40.6	41.3	40.4	41.3	40.4	41.3	40.4	41.3	40.4	41.3	40.4	41.3	40.4	41.3	40.4
CFOV [km]	52.8	40.2	40.9	40.4	40.1	40.7	39.7	40.7	40.3	41.0	40.4	40.6	39.0	40.6	40.2	40.8
Cell-weight [%]	52.6		66.1		68.2		68.5		69.1		69.4		68.6		68.6	
Coast-wt. [%]	7.4		3.1		0.5		0.3		0		0		0.2		0.1	
NRF	2.505		0.517		0.156		0.148		0.144		0.143		0.144		0.142	
CIF	3.339		1.07		0.545		0.515		0.499		0.497		0.503		0.501	
N	76		72		99		88		63		63		65		76	
N-track, N-scan	13	7	10	9	7	18	7	17	5	15	5	15	5	15	5	17

25 km HCS	Channel designation															
	6H		10H		18H		36H		60HV		89H		166H		183HA	
RFOV [km]	--	--	34.4	25.4	25.8	25.2	25.8	25.2	25.8	25.2	25.8	25.2	25.8	25.2	25.8	25.2
CFOV [km]	--	--	35.9	26.1	25.6	25.2	24.3	25.5	22.7	25.4	22.2	25.4	23.9	25.5	22.9	25.4
Cell-weight [%]	--		49.2		66.1		67.1		65.6		65.6		66.7		65.9	
Coast-wt. [%]	--		10.3		2.6		2.2		0.5		0.1		1.8		0.7	
NRF	--		2.94		0.354		0.28		0.24		0.234		0.256		0.244	
CIF	--		3.587		0.912		0.733		0.649		0.637		0.686		0.66	
N	--		54		47		39		29		29		36		29	
N-track, N-scan	--	--	9	8	5	12	5	11	3	11	3	11	5	11	3	11

20 km HCS	Channel designation															
	6H		10H		18H		36H		60HV		89H		166H		183HA	
RFOV [km]	--	--	--	--	24.6	20.5	20.6	20.2	20.6	20.2	20.6	20.2	20.6	20.2	20.6	20.2
CFOV [km]	--	--	--	--	24.8	20.8	18.5	20.3	17.6	20.4	17.5	20.3	17.3	20.3	18.1	20.3
Cell-weight [%]	--		--		55.2		65.7		65.8		65.8		65.5		66.2	
Coast-wt. [%]	--		--		5.6		2.6		2.5		2.2		2.7		2.5	
NRF	--		--		0.44		0.418		0.328		0.311		0.357		0.34	
CIF	--		--		1.002		0.947		0.776		0.742		0.829		0.805	
N	--		--		41		25		23		23		23		23	
N-track, N-scan	--	--	--	--	5	11	3	9	3	9	3	9	3	9	3	9

15 km HCS	Channel designation															
	6H		10H		18H		36H		60HV		89H		166H		183HA	
RFOV [km]	--	--	--	--	24.5	16.2	17.5	15.3	15.9	15.5	16.3	15.5	15.5	15.1	16.9	15.5
CFOV [km]	--	--	--	--	24.7	17.4	16.9	15.4	15.3	15.3	15.4	15.2	14.8	15.0	16.2	15.3
Cell-weight [%]	--		--		41.6		58.8		64.4		63.5		66.1		61	
Coast-wt. [%]	--		--		14.5		4.9		1.7		3.3		2		2.6	
NRF	--		--		0.573		0.601		0.498		0.449		0.576		0.489	
CIF	--		--		1.055		1.145		0.985		0.906		1.1		0.978	
N	--		--		37		19		17		17		17		18	
N-track, N-scan	--	--	--	--	5	10	3	7	3	7	3	7	3	7	3	7

### 2.5.5. Constraints, limitations, and assumptions

- Modeled antenna patterns frozen from the November 2000 design were used in these analyses. Any further design changes may require revision of the performance estimates. Inexact fabrication of the antennas is expected to increase footprint sizes by up to 5% (in terms of IFOV size). Assuming that the composite pattern weighting coefficients are held constant, then this degradation will impact only the spatial features of the composite pattern and not the noise calculations. Otherwise, re-evaluation of the resolution-noise trade-off will be required.
- We have assumed that the 23 GHz patterns are designed to be close to the 18 GHz pattern and that the patterns used are otherwise representative of their channel group.

## 3. Gridding

### 3.1. Background perspective of proposed algorithm

The problem of interpolation of data present on either a grid, or irregularly spaced locations, to a set of grid points has been the subject of study for a long time in meteorology. Typically, fields are undersampled in meteorology, and diverse methods have been devised to spread information to all grid points in the neighborhood of observations. A review of a number of different methods is given in Daley (1991) and Thiebaut and Pedder (1987). We only briefly sketch the different approaches here.

#### *Surface Fitting*



Early methods were based on surface fitting, in which functional forms (e.g., polynomial expansions) were fitted to the available observations. Functional fitting can be done either locally (different functions are used for different analysis grid points) or globally (a single functional form is fitted to all observations in the domain of interest). With either approach, there can be serious problems of underfitting (fewer degrees of freedom in the functional form than in the data, leading to a poor fit to the data) or overfitting (more degrees of freedom in the functional form than in the data, leading to a poor analysis in data-sparse areas).

### *Distance weighting schemes*

This encompasses a large number of techniques that compute analyzed values from a weighted average of surrounding observations. The weights are specified a priori based on the distance between the analysis grid point and the observation. Typically, these techniques employ successive passes, with decreasing length scales of the weighting functions. The two most commonly used techniques are the Cressman (also called the successive correction method) and Barnes schemes, which differ in the functional form of the weighting functions (the Barnes scheme uses a Gaussian weighting function). In their original formulations, the Cressman scheme makes use of a background field (an a priori estimate from another source such as climatology or a short-term forecast), whereas the Barnes scheme does not.

The choice of the adjustable parameters of these techniques has been the subject of extensive study, and methods have been devised for the Barnes scheme to select weighting functions based on either the average data spacing (Koch et al. 1983) or the correlation length scale of the field to be analyzed (Seaman 1989).

There are well-known limitations to these distance-weighting schemes: Anisotropic distributions of observation can lead to unrealistic analyzed values at the edge of data swaths, since the weight given to the observations does not take into account the observation locations relative to each other.

### *Statistical interpolation, variational techniques*

More recently developed methods explicitly take into account the error statistics of the observations (and background field). In statistical interpolation, the weights given to the observations are determined by minimizing the estimated analysis error. In 3dvar and 4dvar techniques, an analyzed field is derived by minimizing a cost function that measures the appropriately weighted misfit to the observations and the background. These methods are usually implemented in the context of an NWP data assimilation system, and require a much larger computational and scientific infrastructure than simpler regridding techniques.

Lorenc (1992) compared the theoretical basis and performance of statistical interpolation with those of iterative schemes (like the successive correction method). He showed that under certain conditions iterative schemes can approximate the results of the statistical interpolation method. He further showed the near-equivalence of employing a recursive filter on the analysis increments to explicitly taking into account the error covariance of the background error. We describe the recursive filter in more detail below.

### 3.2. Algorithm description

The recursive filter is described in Hayden and Purser (1988, 1995, hereafter referred to as HayP88 and HayP95). It was especially designed to provide a computationally efficient interpolation method capable of producing realistic results for datasets with spatial inhomogeneities of coverage.

Its basic computational steps for a single pass of the analysis may be summarized as follows:

- Background values are interpolated to observation location using bilinear interpolation.
- The observation increments (observed value - interpolated background) are then spread to the surrounding four grid points using the adjoint of the bilinear interpolation operator.
- The resulting field of increments is then smoothed through repeated application of a digital filter.

It can be shown that in the implementation used in HayP95, the spectral response of this filter asymptotically approaches that of the Barnes analysis, but with a spatially varying length scale that depends on data density.

HayP95 provide examples and guidance for choosing the adjustable parameters of the filter. The filter has been widely used in the processing of satellite data; it has also been used in the context of 4dvar assimilation systems in the estimation of the background error covariance matrix.

#### *Formulation*

The analysis scheme is similar to a successive correction method, where at iteration  $n+1$  the analysis values  $A(n+1)$  are given by equation (13) of HayP95:

$$A(n+1) = A(n) + \frac{G^* [W(O - A(n))]}{G^* W} \quad (19)$$

where  $O$  indicates observed values,  $W$  the product of quality and observation weights,  $W_b$  the weight given to the background field, and  $A_b (=A(0))$  indicates the background (or first guess) field. The operator  $G^*$  indicates the distribution and smoothing of values from the observation points to the analysis grid points.

The operator  $G^*$  is implemented in two stages—an interpolation step and a smoothing step. In the interpolation step values at observation points are distributed to the neighboring four analysis grid points using the adjoint of a bilinear interpolation formula. Contributions from all observations are added to each applicable grid point. The formula for the sum in one dimension at a single grid point is given by equation (12) of HayP95:

$$X_i = \sum_{k: |dx_k| < \delta}^K \left( 1 - \frac{|dx_k|}{\delta} \right) \hat{X}_k \quad (20)$$
$$\hat{X}_k = \hat{W}_k (\hat{O}_k - \hat{A}_k)$$

where  $dx_k$  is the distance between observation  $k$  and the grid point, and  $\delta$  is the grid spacing (only observations within  $\delta$  are considered in the sum). The values of  $A$  at the observation points  $k$  are

obtained by bilinear interpolation from the surrounding analysis points. An entirely analogous operation is performed for the quality weights  $W$  (more on the definition of  $W$  below). The smoothing step, in a horizontal implementation, is a two-dimensional smoother which is applied one or more times, both to the weights ( $W$ ) and weighted residuals ( $W(O-A)$ ). The filter consists of a forward and reverse filter applied in both horizontal dimensions. The fundamental filter equation for one dimension is given by equation (1) of HayP95:

$$A'_i = \alpha A'_{i-1} + (1 - \alpha) A_i, \quad 0 < \alpha < 1 \quad (21)$$

where  $A$  is the input field,  $A'$  the output, and  $\beta = (1 - \alpha)$  is the smoothing parameter that controls the spatial scale of the filter. The corresponding equation for the reverse filter is given by HayP95 equation (4):

$$A''_i = \alpha A''_{i+1} + (1 - \alpha) A'_i \quad (22)$$

The result of  $L$  iterations of the filter (21) and (22) asymptotically approaches that of a single application of a Gaussian filter given by HayP95 equation (9):

$$G_j \approx G_o \exp \left[ -\frac{|j|^2}{2L(\lambda\delta)^2} \right] \quad (23)$$

$$G_o \approx \frac{1}{[2\pi(L\lambda^2)]^{\frac{1}{2}}},$$

with length scale  $R$  given by HayP95 equations (10) and (11):

$$R^2 = 2L(\lambda\delta)^2 \quad (24)$$

$$R^2 = \frac{2L\alpha\delta^2}{(1 - \alpha)^2}, \quad (25)$$

The  $L$  and  $\delta$  are constants,  $R$  is prescribed for the analysis pass, and  $\beta = (1 - \alpha)$  is obtained by inverting (25). The variable scaling is obtained by allowing the  $R$  to be defined separately for each pass and for each grid point. Details are given in HayP95 equations (14)-(17).

The observation quality weights ( $W$ ) are defined as the product of an a priori reliability estimate (between 0 and 1, initialized to a nominal value of 1 in the absence of ancillary information about data quality), and a quality estimate based on a scaled difference between the observation and the analysis from a previous pass. See HayP95 equations (18) and (19) for details.

### Implementation

There are several parameters of this analysis scheme that must be specified and tuned. HayP95 (Table C1 in their Appendix C) provide a set of default values for all of the parameters, derived from a set of three adjustable parameters: The grid length  $\delta$ , a smoothing parameter  $f$ , and the tolerance  $Tol$  used in the definition of the quality estimate. We outline the steps of our proposed implementation in the following:

- (1) *Select filter parameters*: Select  $\delta$  based on the output grid spacing, and use the default values for  $f$  ( $=1$ ) and  $Tol$  ( $=1$ ).
- (2) *Perform initial background analysis*: A preliminary analysis is performed using one analysis pass ( $M=1$ ), with a characteristic scale of four grid increments, and all other parameters as given in table C1 of HayP95. The individual steps of this analysis pass are the following:
  - (2.1) Interpolate prior analysis to observation locations: For the initial analysis only, this step can be omitted, since there is no prior analysis (i.e., it is identically zero).
  - (2.2) Interpolate weight to observation locations: For the initial analysis only, this step can also be omitted, since it is identically unity.
  - (2.3) Evaluate  $G*W$  and  $G*(W(O-A))$ : This involves both the interpolation (20) and smoothing steps ( $L$  iterations of (21) and (22)).
  - (2.4) Update the analysis using (19).
- (3) *Perform final analysis*: Using the output from step 2 as the prior analysis, perform the final data analysis using five analysis passes with  $L=3$  iterations of the smoother each. The characteristic scale of the filter is decreased from  $6\delta$  to  $\delta$  over the five analysis passes, with all other parameters given in table C1. Each analysis pass encompasses the individual steps outlined for step 2.

The parameter choices given above are our baseline values. Some tuning will be necessary to optimize the performance of the regridding algorithm for grid spacing, data density and distribution, and spectral characteristics of the sensor parameters. Subjective evaluation of the analyzed fields and objective methods (comparison against withheld data values) will be used in assessing the performance of the regridding algorithm.

### 3.3. Algorithm Performance

HayP95 give several examples of the successful application of the filter:

- A surface temperature analysis over the continental US and adjoining oceans, which is a difficult field because of the rapid changes in observed values due to topography, and rapidly varying data density at the coast line
- An analysis of 500 hPa height over North America and the North Pacific using gradient wind estimates from VAS retrievals of temperature and moisture. Data density in this case was high in isolated patches, surrounded by large data-void areas.

A version of the recursive filter was also in operational use the UK Meteorological Office for producing their operational analyses.

## 4. Imagery EDR

### 4.1. Objectives

The imagery EDR complements the environmental EDR products. Because the imagery brightness temperatures are equivalent to the EDR algorithm input values, the imagery EDR facilitates visualization of processes at work in the EDR source data as well as reprocessing using user-defined alternatives to the EDR algorithms. Imagery is also potentially useful for phenomenon location (e.g., storm centers) and tracking (bulk sea ice motion), detection and monitoring of transient signals (e.g., RFI), and data quality verification.

## 4.2. SRD Requirements

The text below and Table 4-1 are the portions of CMIS SRD section 3.2.1.1.1.1 that apply directly to the Imagery EDR.

### Imagery

### TRD App D Section 40.2.3

Brightness temperature data from each microwave channel shall be available for display at the sampled resolution. The threshold horizontal spatial resolution (HSR) is to be consistent with the performance of the related EDRs. The display capability for all imagery should be consistent with the dynamic range of any CMIS channel

**Table 4-1: SRD Requirements for the Imagery EDR**

Para. No.		Thresholds	Objectives
	a. Horizontal Spatial Resolution		
C40.2.3.1-1	1. Global	Consistent with related EDRs	(TBD)
C40.2.3.1-2	b. Horizontal Reporting Interval	Consistent with related EDRs	(TBD)
C40.2.3.1-3	c. Horizontal Coverage	Global	Global
C40.2.3.1-4	Not Used		
C40.2.3.1-5	d. Measurement Range	Dynamic range of all measurement channels	Dynamic range of all measurement channels
C40.2.3.1-6	e. Measurement Uncertainty (TBR)	Derived	Derived
C40.2.3.1-7	f. Mapping Uncertainty	3 km (TBR)	(TBD)

In addition to these requirements, the SRD specifies:

1. “Science algorithms shall process CMIS data, and other data as required, to provide the [EDRs] assigned to CMIS.” (SRD, paragraph SRDC3.1.4.2-1)
2. “Specified EDR performance shall be obtained for any of the orbits described in paragraph 3.1.6.3 ...” (SRDC3.1.6.3-2)
3. “As a minimum, the EDR requirements shall be satisfied at the threshold level.” (SRDC3.2.1.1.1-3)
4. “... the contractor shall identify the requirements which are not fully satisfied, and specify the conditions when they will not be satisfied.” (SRDC3.2.1.1.1-4)
5. “... CMIS shall satisfy the EDR Thresholds associated with cloudy conditions under all measurement conditions ...” (SRD SRDC3.2.1.1.1-1)

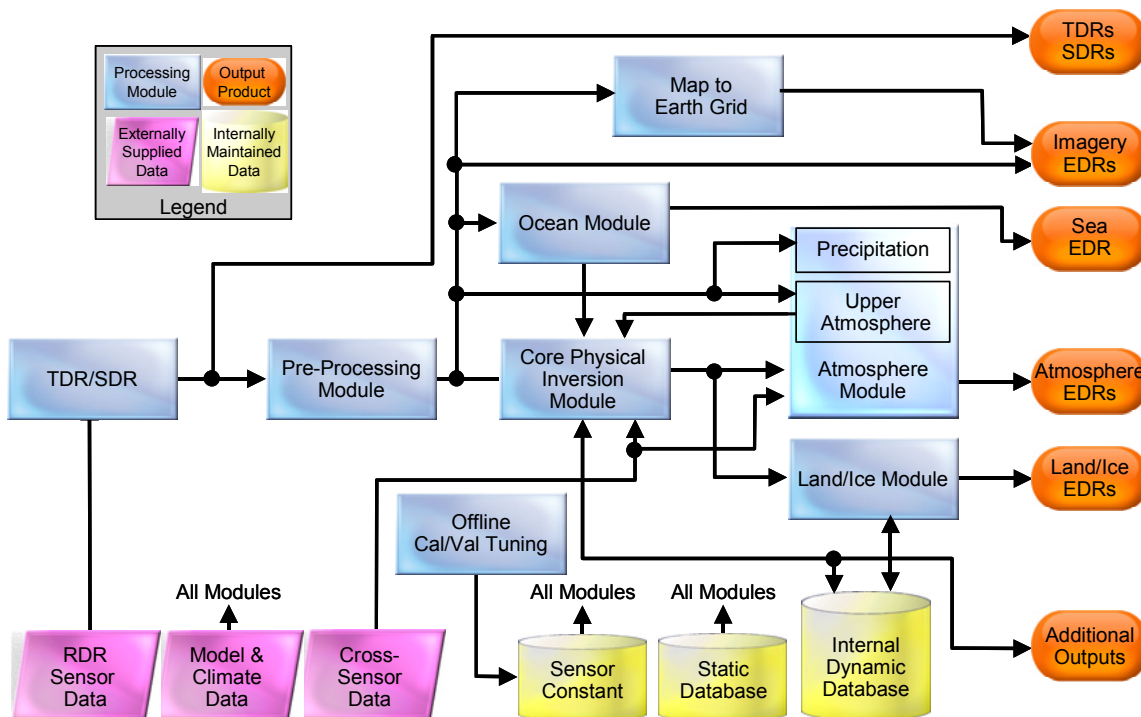
Also note that the CMIS system consists “of all ground and spaceborne hardware and software necessary to perform calibrated, microwave radiometric measurements from space and the software and science algorithms necessary to process ... these measurement into a format consistent with the requirements of the assigned [EDRs].” (SRD, section 3.1.1)

## 4.3. Algorithm description

Figure 4-1 shows the CMIS processing flow leading to the generation of data for the Imagery EDR. TDR/SDR processing is discussed in the *ATBD for CMIS TDR/SDR Algorithms*. The EDR pre-processing module includes footprint matching (described in section 2 above) and radiative transfer model (RTM) calibration of SDR data which removes biases derived post-launch (also described in the *ATBD for CMIS TDR/SDR Algorithms*.) The output of the pre-processing module is empirically-corrected brightness temperature (ECBT). The earth-gridding process is described in section 3 (above). The earth-grid definition is a user-definable input to

the gridding process. Candidate grids include those defined for the National Snow and Ice Data Center's (NSIDC) Equal-Area SSM/I Earth Grid (EASE-Grid, <http://nsidc.org>) modified to meet the horizontal reporting interval requirements for the various EDRs. As with EASE-Grid—which has global-cylindrical, north-azimuthal, and south-azimuthal grid projections—multiple earth projections will be used to provide global coverage while optimizing EDR product usability.

**Figure 4-1: Overall CMIS processing flow including Imagery EDR**



#### 4.4. Algorithm Performance

Table 4-2 gives the nominal performance characteristics for the imagery EDR. The table gives nominal HSR performance values—typically equal to the EDR horizontal cell sizes—whereas section 2.5 above provides estimated composite footprint performance per each channel and horizontal cell size combination. Imagery data for each channel is provided at *every* EDR resolution where a high-fidelity footprint match can be made. Table 4-3 lists the few exceptions where the sensor footprints are too large to report useful imagery data for some of the EDR resolutions. Detailed analysis of composite footprint processing and the associated noise and spatial match trade-offs are given in section 2.5.

**Table 4-2: Imagery EDR nominal performance**

Para. No.		Thresholds	Objectives	Performance
	a. Horizontal Spatial Resolution			
C40.2.3.1-1	1. Global	Consistent with related EDRs	(TBD)	15, 20, 25, 40, 50, and 56×35 km
C40.2.3.1-2	b. Horizontal Reporting Interval	Consistent with related EDRs	(TBD)	15, 20, 25, 40, 50, and 56×35 km
C40.2.3.1-3	c. Horizontal Coverage	Global	Global	Global
C40.2.3.1-4	Not Used			
C40.2.3.1-5	d. Measurement Range	Dynamic range of all measurement channels	Dynamic range of all measurement channels	Dynamic range of all measurement channels
C40.2.3.1-6	e. Measurement Uncertainty	Derived	Derived	Derived
C40.2.3.1-7	f. Mapping Uncertainty	3 km (TBR)	(TBD)	3 km

**Table 4-3: Imagery EDR excluded conditions**

Exclusion	Rationale
6 GHz at spatial resolution < 50 km	Sensor resolution is flowed from requirements for category 1 and 2 EDRs and does not support creating imagery for this channel at higher resolution without substantial noise amplification
10 GHz at spatial resolution < 40 km	Sensor resolution is flowed from requirements for category 1 and 2 EDRs and does not support creating imagery for this channel at higher resolution without substantial noise amplification
18 and 23 GHz at spatial resolution < 20 km	Sensor resolution is flowed from requirements for category 1 and 2 EDRs and does not support creating imagery for this channel at higher resolution without substantial noise amplification

## 5. Glossary of Acronyms

AMSR	Advanced Microwave Scanning Radiometer
ATBD	Algorithm Theoretical Basis Document
AVHRR	Advanced Very High Resolution Radiometer
BT	Brightness Temperature [K]
CIF	Calibration input factor
CFOV	Composite field-of-view
CMIS	Conical Microwave Imaging Sounder
COS	Center of scan
DEM	Digital Elevation Model
DMSP	Defense Meteorological Satellite Program
EFOV	Effective field-of-view
EDR	Environmental Data Record
EIA	Earth Incidence Angle
EOS	Edge of scan
ESMR	Nimbus-7 Electrically Scanning Microwave Radiometer
FOR	Field of Regard
FOV	Field Of View

IFOV	Instantaneous Field Of View
LST	Land Surface Temperature [K]
NPOESS	National Polar-orbiting Operational Environmental satellite System
NRF	Noise reduction factor
RFI	Radio-Frequency Interference
RFOV	Reference field-of-view
RMS	Root Mean Square
RMSE	Root Mean Square Error
SDR	Sensor Data Record
SSM/I	Special Sensor Microwave/Imager
SSMIS	Special Sensor Microwave Imager Sounder
TB	Brightness Temperature
TMI	TRMM Microwave Imager
TOA	Top-of-Atmosphere (i.e., measured by sensor)
TRMM	Tropical Rainfall Measuring Mission
USGS	United States Geological Survey
VIIRS	Visible/Infrared Imager/Radiometer Suite
VIRS	Visible and Infrared Radiometer System (on TRMM)
VST	Vegetation/Surface Type
VWC	Vegetation Water Content [kg/m <sup>2</sup> ]

## 6. References

### 6.1. Technical Literature

- Backus, G., and F. Gilbert, Uniqueness in the inversion of inaccurate gross earth data, *Phil. Trans. Roy. Soc. London*, A266:123-192, 1970.
- Daley, R., *Atmospheric Data Analysis*. Cambridge University Press, 1991.
- Farrar, M. R., and E. A. Smith, Spatial resolution enhancement of terrestrial features using deconvolved SSM/I brightness temperatures, *IEEE Trans. Geosci. Rem. Sens.*, 30(2):349-355, 1992.
- Hayden, C. M., and R. J. Purser, Three-dimensional recursive filter objective analysis of meteorological fields. *CIMSS View*, 4:1-5, 1988
- Hayden, C. M., and R. J. Purser, Recursive filter objective analysis of meteorological fields: applications to NESDIS operational processing. *J. Appl. Meteor.*, 34:3-15, 1995
- Lorenc, A., Iterative analysis using covariance functions and filters. *Quart. J. Roy. Meteor. Soc.*, 118:569-591, 1992
- Panegrossi, G., A. Tassa, S. Di Michele, G. J. Tripoli, A. Mugnai, E. A. Smith, Using TRMM observations to improve numerical simulations of precipitation within tropical cyclones, Proc. Of Symposium on Precipitation Extremes: Prediction, Impacts, and responses, *81 AMS Meeting*, Albuquerque, NM, pp. 324-326, 2001.
- Poe, G. A., Optimum interpolation of imaging microwave radiometer data, *IEEE Trans. Geosci. Rem. Sens.*, 28(5):800-810, 1990.
- Seaman, R. S., Tuning the Barnes objective analysis parameters by statistical interpolation theory. *J. Atmos. Ocean. Technol.*, 6:993-1000, 1989
- Stogryn, A., Estimates of brightness temperatures from scanning radiometer data, *IEEE Trans. Ant. and Prop.*, AP-26(5):720-726, 1978.
- Thiebaux, H. J., and M. A. Pedder, *Spatial Objective Analysis: With Applications in Atmospheric Science*. Academic Press, London, 1987.
- Tripoli, 1992a: A nonhydrostatic model designed to simulate scale interaction, *Mon. Wea. Rev.*, 120, 1342-1359.



Tripoli, 1992b: An explicit three dimensional nonhydrostatic numerical simulation of a tropical cyclone. *Meteor. Atmos. Phys.*, 49, 229-254.

Tripoli et al., 2000: Orographically induced flash floods on the northern Italian coast, Ninth Conference on Mountain Meteorology, *AMS*, Aspen, CO, 336-339.

## 7. Appendix A — EFOV plots

The following figures are plots of the EFOV patterns of the representative channels at the center-of-scan and 833 km altitude. The y-axis is across-scan distance and the x-axis is along-scan.

**Figure 7-1: 6, 10, 18, and 36 GHz effective footprint patterns**

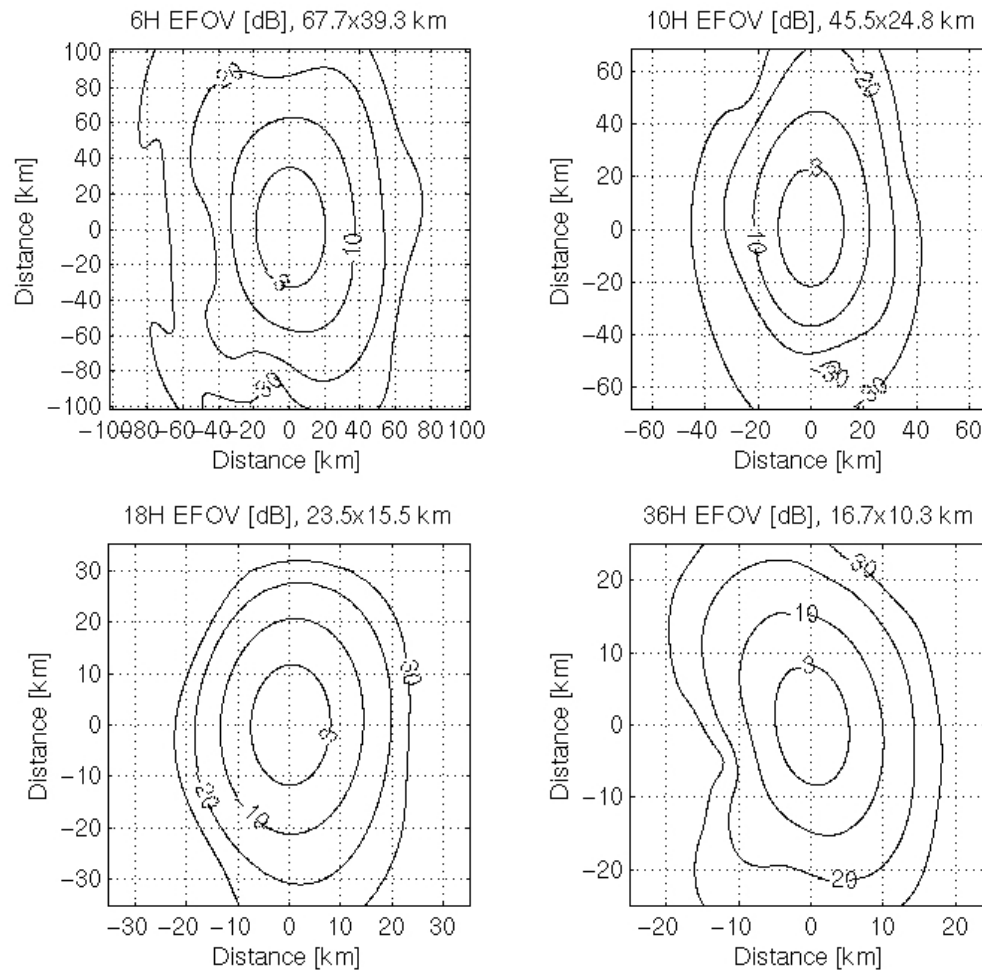


**Figure 7-2: 60, 89, 166, and 183 effective footprint patterns**

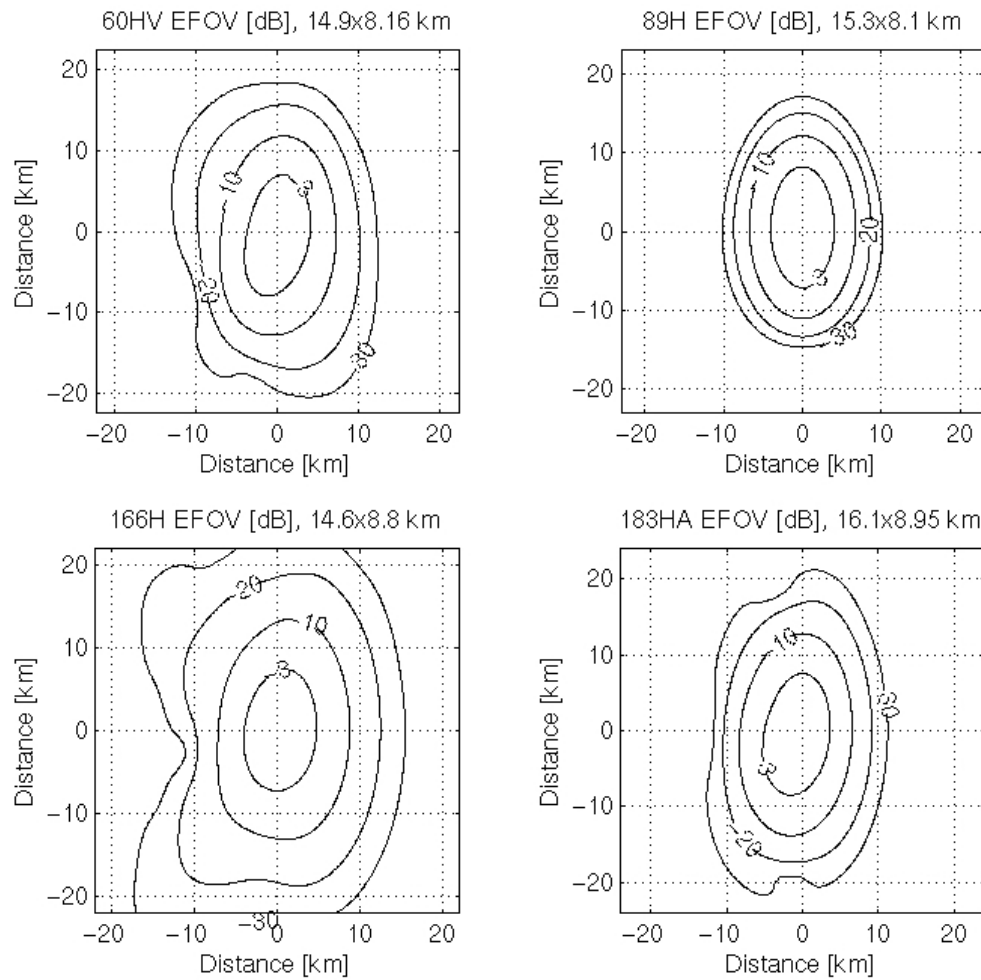
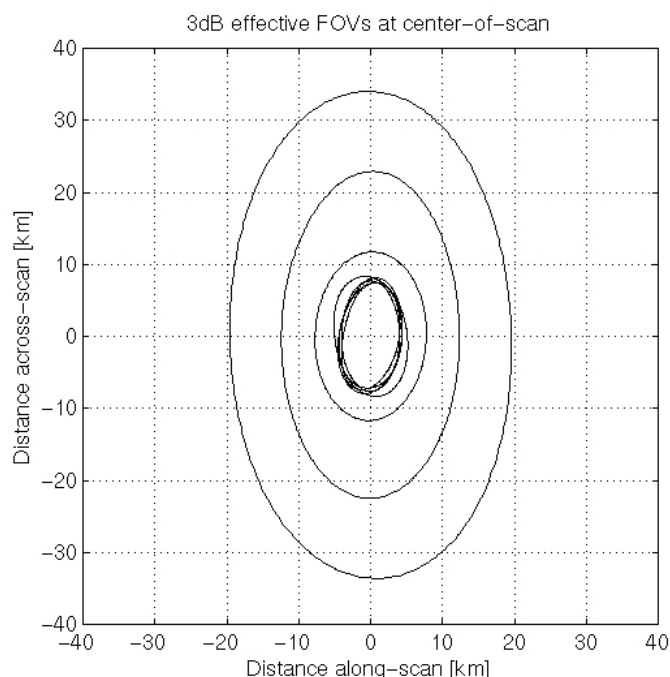


**Figure 7-3: EFOVs plotted at center-of-scan to show coincidence**



## **8. Appendix B — Earth rotation**

The following slides discuss the effect of earth rotation on footprint matching. Note that the scan pattern analyzed is somewhat different from the one presented above. Earth rotation could be considered in footprint matching calculations but it would require the calculation and storage of many additional weighting coefficient sets to be applied depending on spacecraft latitude. In summary, the analysis suggests that even in the worst case near the equator, the effect is small enough to neglect.



# Footprint Matching with Earth Rotation



- **Problem to be addressed**
  - **Earth rotation distorts the distribution of sensor footprints relative to the distribution projected on a non-rotating earth**
  - **Impacts**
    - » **Footprint matching: A non-rotating earth is normally assumed so that a single interpolation coefficient set may be used globally**
      - Requiring latitude-dependent coefficients would increase computer memory needs and processing time
    - » **Collocation: Relative positions of channels on different scan lines (EIA) would change with latitude**

Channel [GHz]	6.8	10.7	18.7	23.5	37	56	88	166	183
Relative range to scan [km]	63.2	140	0	0.13	63.2	63	62.6	62.1	61.2
Range to scan [#sensor scans]	5.1	11.2	0	0	5.1	5.0	5.0	5.0	4.9
Time to scan [s]	2.7	5.9	0	0	2.7	2.7	2.6	2.6	2.6
X-track motion at equator [km]	2.4	5.2	0	0	2.3	2.3	2.3	2.3	2.3

For Official Use Only/HSC Competition Sensitive

Source Selection Information  
See FAR 3.104

Section number -2

For Official Use Only/HSC Competition Sensitive



# Footprint Matching with Earth Rotation



- **Proposed footprint matching procedure**
  - **Define high-density (i.e. 2 km) interpolation grid in non-rotating sensor-based coordinate system**
    - » **Interpolation coefficients for this grid are calculated only once**
    - » **High-density grid minimizes geolocation error**
  - **Define composite footprint loci with respect to the main scan**
    - » **37-88 GHz are coincident with loci, 166-183 are nearly coincident**
      - Footprint matching/interpolation has minimal geolocation error
    - » **6.8-23.5 GHz must be interpolated to composite footprint loci**
      - Select interpolation points on-the-fly from high-density grid
      - Geolocation error is less than 0.71 x grid spacing
  - **Interpolate/footprint match using global coefficient sets defined for non-rotating earth**
    - » **Global coefficient use does not add to geolocation error**
    - » **Global coefficient use does distort composite footprint shape**

For Official Use Only/HSC Competition Sensitive

Source Selection Information  
See FAR 3.104

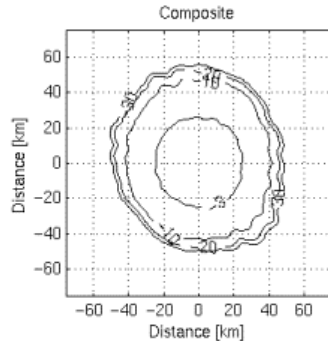
Section number -3



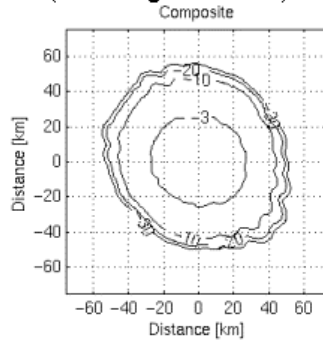
- **Sensor: 88 GHz. HCS: 50 km. Scan position: 5% (from edge).**

	a-track	x-track	%HCS	%coast
– No rotation:	51.2	49.5	63.4	0.1
W/rotation:	51.8	54.1	60.2	0.1

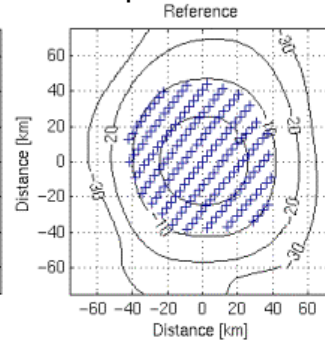
Composite with  
no earth rotation



Comp. realized at equator  
(left-to-right rotation)



Reference with  
sample locations



Source Selection Information  
See FAR 3.104

For Official Use Only/HSC Competition Sensitive

Section number-5

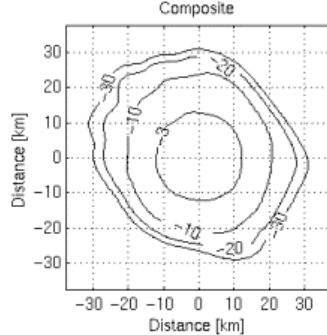
For Official Use Only/HSC Competition Sensitive



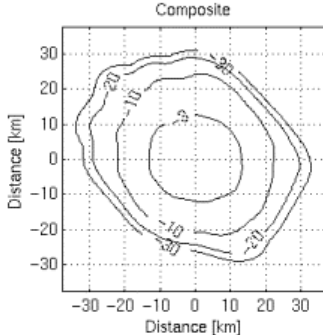
- **Sensor: 88 GHz. HCS: 25 km. Scan position: 5% (from edge).**

	a-track	x-track	%HCS	%coast
– No rotation:	25.1	24.4	62.5	0.4
W/rotation:	25.2	26.4	59.5	0.4

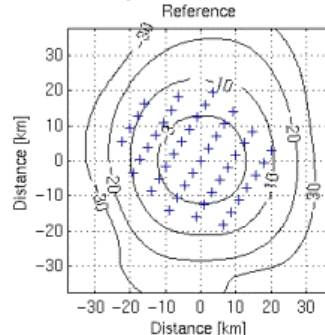
Composite with  
no earth rotation



Comp. realized at equator  
(left-to-right rotation)



Reference with  
sample locations



Source Selection Information  
See FAR 3.104

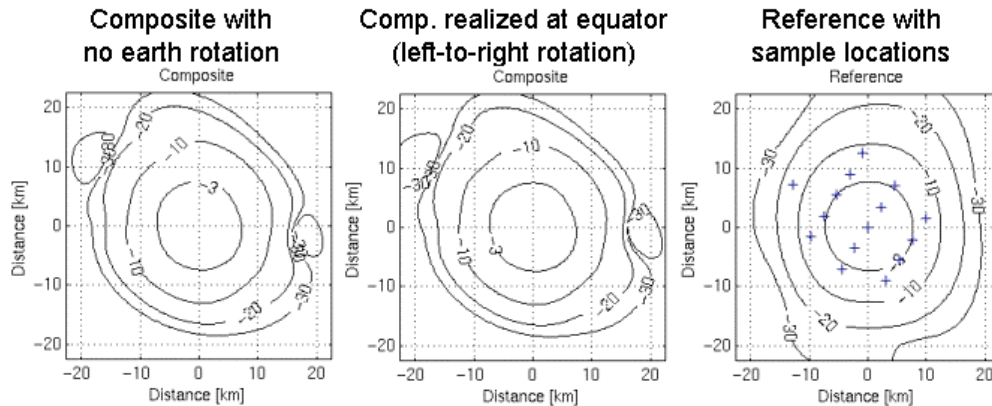
For Official Use Only/HSC Competition Sensitive

Section number-6



- **Sensor: 88 GHz. HCS: 15 km. Scan position: 5% (from edge).**

	a-track	x-track	%HCS	%coast
– No rotation:	15.0	14.4	61.6	1.2
– W/rotation:	15.0	14.7	61.0	1.2



Source Selection Information  
See FAR 3.104

For Official Use Only/HSC Competition Sensitive

Section number-7

## 9. Appendix C — Errors due to the horizontal interpolation of EDRs

### 9.1. Recursive Filter Methodology and Formulas

Regridding from the input FOVs to the output locations is performed using the recursive filter (see section 3.2 for a discussion of the recursive filter). The resulting interpolation errors are estimated here by approximating its effects as those of a Gaussian filter. The two-dimensional recursive filter, when applied a number of iterations, approximately corresponds to a Gaussian filter with weights proportional to

$$w(x) = \exp\left(\frac{-x^2}{R^2}\right), \quad (C-1)$$

where  $R$  depends on the data density and the analysis pass. In the configuration recommended by HayP95,  $R$  at a given grid point ( $R_i$ ) is obtained from

$$R_i = \frac{f\delta}{\sqrt{(W_i)}}, \quad (C-2)$$

subject to the constraint that

$$R_m < R_i < R_0, \quad (C-3)$$

where  $f$  is an adjustable parameter,  $\delta$  is the grid spacing, and  $W_i$  is the local sum of data quality weights,  $R_0$  is the specified maximum value of  $R$ , and  $R_m$  is a minimum value specified for each analysis pass. The sum of weights is obtained by the formula

$$W_i = \sum_k \left(1 - \frac{|d_k|}{\delta}\right) W_k, \quad (C-4)$$

where  $d_k$  is the distance between observation  $k$  and grid point  $i$ , and  $W_k$  is a data quality weight assigned to observation  $k$ , and the sum is accumulated over all  $k$  for which  $|d_k| < \delta$ .

For the case of regridding from one set of approximately regularly spaced points to another, the following simplifications can be made:

$$W_k = 1 \text{ for all } k.$$

If we further choose the output grid no finer than the input grid, the sum of weights  $W_i \geq 1$ . This analysis neglects the effects of missing data in the input grid, because in that case larger smoothing radii are used locally. Using the value  $f=1$  suggested in HayP95 results in  $R_i \leq \delta$  for all grid points  $i$ , which is smaller than the limiting value  $R_m$  suggested in HayP95 for all but the last pass of the analysis. Therefore, the expression for  $R_i$  simplifies to  $R_i = R_m$ . HayP95 suggest 5 analysis passes, with values of  $R_m$  as follows:



Pass	$R_m/\delta$
1	6.0
2	3.5
3	2.1
4	1.3
5	0.9

The passes are applied as successive corrections:

$$A_m = A_{m-1} + G(O - A_{m-1}), \quad (C-5)$$

where  $O$  is the original field,  $A_0=0$ , and  $G()$  represents one pass of the recursive filter analysis.

## 9.2. Error Budget Calculations

### 9.2.1. Methodology

For the purpose of estimating the interpolation error introduced by the recursive filter, we simulate its effect as a series of five successive correction analysis passes given by (C-5), with  $G()$  represented by the Gaussian filter (1) with scale parameter  $R_m/\delta$  for analysis pass  $m$  given by:

$m=1$ : 6.0;      $m=2$ : 3.5;      $m=3$ : 2.1;      $m=4$ : 1.3;      $m=5$ : 0.9.

We note that this filtering is applied to the actual retrieved quantities, which are themselves approximately Gaussian averages, whereas the desired retrieved quantities are averages over square areas. The errors resulting from this mismatch have been separately estimated.

### 9.2.2. Computational Details

We approximate the Gaussian filter by the same truncated quasi-Gaussian filter (TQGF) used in the analysis of sensor averaging errors, with length parameter  $s = R/\delta$ .

The sensor averaging errors were evaluated using a very high resolution input dataset (grid spacing 2.34 km and 2.5 km), and filtered values were computed on a subsampled output grid (every 5 grid points, or roughly 12 km grid spacing). The desired output grid, and the input grid of retrieved values, have a spacing of 12.5 km, which approximately corresponds to the subsampling of every 5 grid point of the high-resolution input dataset used in the sensor-averaging error analysis.

We use the sensor-averaged ( $z_g$ ) and true (square-averaged,  $z_s$ ) quantities on this 12 km grid, and then apply the recursive filter to the sensor-averaged gridded values ( $z_g$ ) to obtain interpolated values ( $z_{rf}$ ). For single values, the aggregate error  $E_a$  of the combined effects of sensor averaging and interpolation (filtering) is then obtained as the difference  $E_a = (z_{rf} - z_s)$ , which can be broken down into the components due to sensor averaging ( $E_g$ ) and interpolation ( $E_{rf}$ ) as:

$$\begin{aligned} E_a &= E_{rf} + E_g \text{ with} \\ E_{rf} &= z_{rf} - z_g \text{ and} \\ E_g &= z_g - z_s. \end{aligned}$$

Note that if a breakdown of the error budget in terms of mean square errors (MSE) or error variances is required, possible correlation between  $E_{rf}$  and  $E_g$  must be taken into account. Therefore, defining

$$MSE_a = \left( \frac{1}{N} \right) \sum_{k=1}^N E_{a,k}^2 \quad (C-6)$$

we could define

$$MSE_a = C_g + C_{rf}, \quad (C-7)$$

with contribution  $C_g$  and  $C_{rf}$  given by

$$C_g = MSE_g, \quad \text{and} \quad (C-8)$$

$$C_{rf} = MSE_a - MSE_g. \quad (C-9)$$

For completeness, we also evaluate the statistics of the differences between  $z_g$  and  $z_{rf}$  (which allows determination of the correlation between  $E_{rf}$  and  $E_g$ ).

### 9.2.3. Example Calculations

We illustrate the filtering effects of the recursive filter interpolation for the case of the high-resolution low-level mixing ratio for Bonnie at forecast hour 48. The raw field is shown in Figure 9-1, the corresponding true retrieved (SURF,  $z_s$ ) values in Figure 9-2, and the sensor values (TQGF,  $z_g$ ) on the input grid in Figure 9-3. The recursive filter is applied to this field, with the result ( $z_{rf}$ ) shown in Figure 9-4. Results for the individual passes (not shown) show a progressively higher resolution analysis. In our simulation study, we assumed a uniform data density commensurate with the output grid resolution, in which case the first 4 passes of the recursive filter analysis have little effect (there is little difference between the final analysis of the 5-pass recursive filter outlined above and a single pass of the recursive filter analysis with the smallest length scale  $R$ ). However, all results shown here use the final results of the 5-pass recursive filter analysis. The basic statistics for this case are given below.

**Table 9-1: Statistics for Bonnie low-level mixing ratio (see text)**

	N	bar	sd	rms	min	max
$z_s$	1521	6.35e-03	2.26e-03	6.74e-03	0.001372	0.011280
$z_g$	1225	6.80e-03	2.15e-03	7.13e-03	0.001539	0.011058
$z_{rf}$	1225	6.80e-03	2.14e-03	7.13e-03	0.001604	0.010784
zae	1225	1.06e-06	6.39e-05	6.39e-05	-0.000236	0.000320
zre	1225	-3.90e-04	9.84e-03	9.85e-03	-0.045777	0.044760
rsae	1225	1.08e-06	1.35e-04	1.35e-04	-0.000491	0.000638
rsre	1225	-7.00e-04	2.03e-02	2.03e-02	-0.084502	0.085815
rgae	1225	2.00e-08	7.43e-05	7.43e-05	-0.000260	0.000340
rgre	1225	-3.18e-04	1.12e-02	1.12e-02	-0.048782	0.042979

Here ae and re represent the absolute and relative error, respectively, for the following difference fields:

zae, zre:  $z_s - z_g$  (error introduced through sensor averaging)  
rsae, rsre:  $z_s - z_{rf}$  (aggregate error of sensor averaging and interpolation)  
rgae, rgre:  $z_g - z_{rf}$  (error introduced through interpolation)

In this case the interpolation step introduces an additional error of approximately the same magnitude as the error introduced by the sensor averaging. The aggregate error rms (rsae = 1.4 e-4) is larger than the sum of individual contributions  $\sqrt{rgae^2 + zae^2} = 9.8 \text{ e-5}$ , indicating a positive correlation between the two error components.

**Figure 9-1: The low-level mixing ratio field (kg/kg) for the Bonnie case at forecast hour 48.**

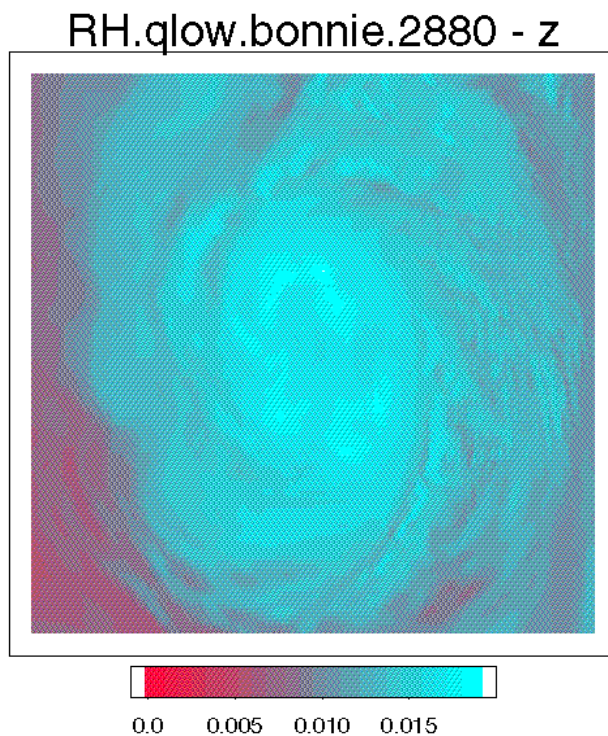


**Figure 9-2: The low-level mixing ratio field (kg/kg) for the Bonnie case at forecast hour 48, filtered with the SURF (true values, zs).**

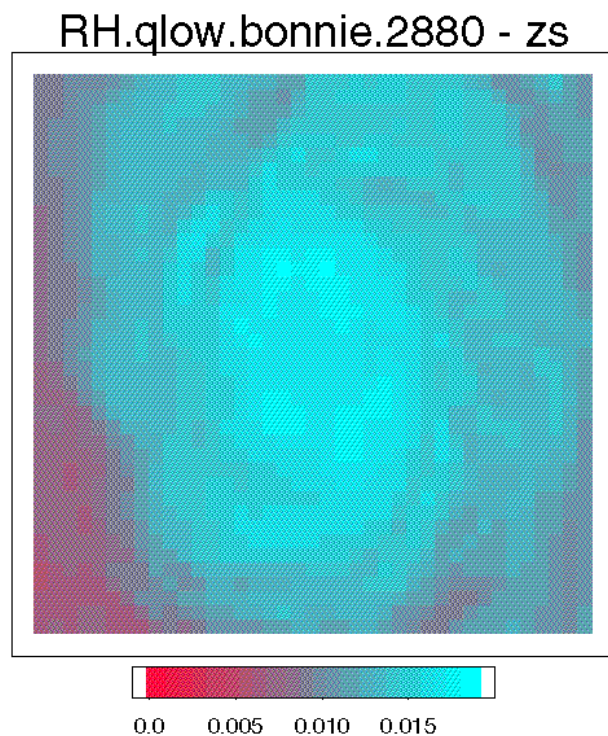


**Figure 9-3: The low-level mixing ratio field (kg/kg) for the Bonnie case at forecast hour 48, filtered with the TQGF (sensor values, zg).**

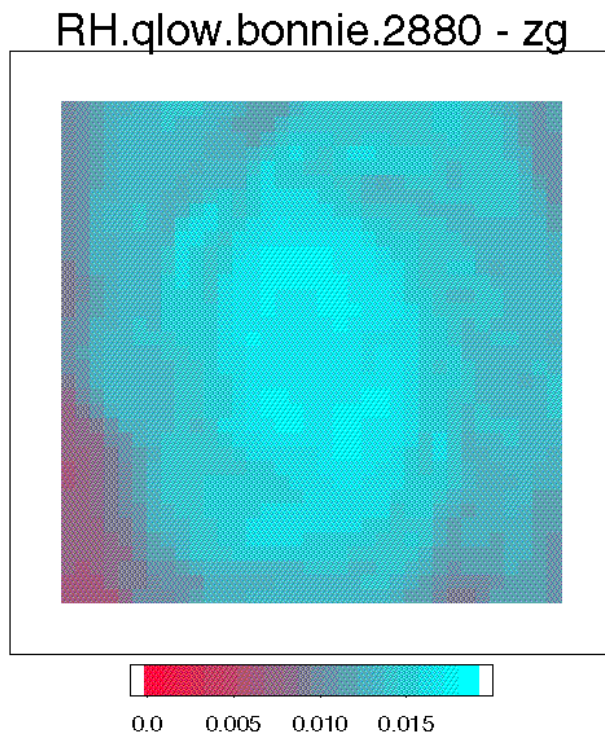
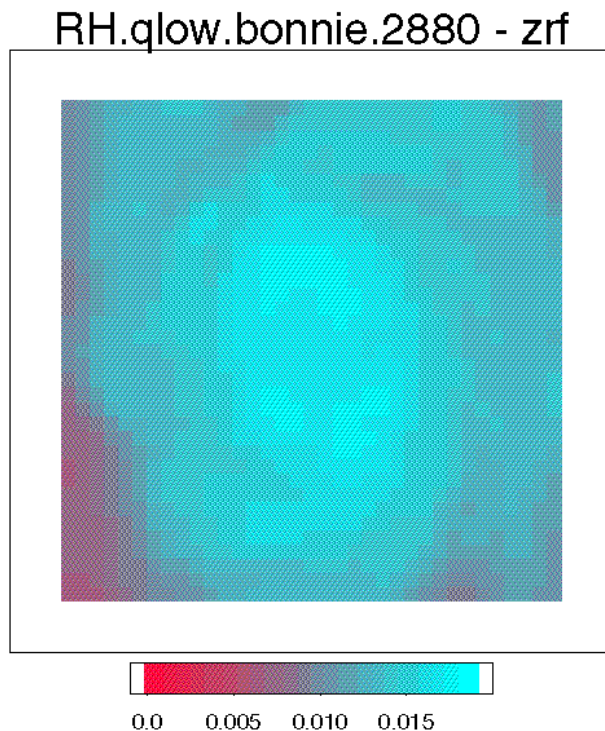


**Figure 9-4: The low-level mixing ratio field (kg/kg) for the Bonnie case at forecast hour 48, filtered with the TQGF and recursive filter (interpolated values, zrf).**



### 9.3. Results for all Cases and Times

We extend the calculations shown in the previous section to all cases (Bonnie, Friuli, and Genoa) and times, for the layer-averaged mixing ratios (low, middle, and high), for the high-resolution (15 km) retrievals. The time-averaged error rms of the absolute error are shown side-by-side for the aggregate (rsae) and component (rgae and zae) errors in the following table.

**Table 9-2: Time-averaged RMS absolute aggregate and component error, all cases**

Case	Var	RMS AE		
		rsae	zae	rgae
Friuli	r(mid)	3.31 e-05	1.71 e-05	1.70 e-05
	r(high)	8.94 e-06	4.67 e-06	4.55 e-06
	r(low)	5.44 e-05	2.78 e-05	2.84 e-05
Genoa	r(mid)	8.39 e-05	4.25 e-05	4.26 e-05
	r(high)	1.76 e-05	8.92 e-06	8.99 e-06
	r(low)	8.32 e-05	4.41 e-05	4.19 e-05
Bonnie	r(mid)	1.72 e-04	8.14 e-05	9.42 e-05
	r(high)	8.36 e-05	3.91 e-05	4.60 e-05
	r(low)	2.36 e-04	1.13 e-04	1.29 e-04

The corresponding time-averaged error rms statistics for the relative error are shown in the following table.

**Table 9-3: Time-averaged RMS relative aggregate and component error, all cases**

Case	Var	100*RMS RE		
		rsae	zae	rgae
Friuli	r(mid)	1.49	0.81	0.78
	r(high)	2.71	1.47	1.39
	r(low)	0.76	0.39	0.40
Genoa	r(mid)	2.48	1.29	1.28
	r(high)	4.21	2.33	2.22
	r(low)	0.94	0.51	0.48
Bonnie	r(mid)	2.54	1.23	1.42
	r(high)	4.93	2.47	2.93
	r(low)	1.83	0.89	1.01

Both tables show a pattern that is consistent with the results shown for the example calculation shown in the previous section: the interpolation errors as simulated here by the smoothing of the sensor-averaged fields are of the same order as those introduced by the sensor averaging pattern, leading to aggregate rms errors about twice as large as those resulting from the sensor averaging alone. Time-averaged rms aggregate errors are less than 5% for any of the cases for r(high), less than 3% for r(mid), and less than 2% for r(low).

#### 9.4. Discussion/Conclusions

Regridding of retrieved values from a set of input FOVs to a set of output locations (at comparable spatial resolution) is performed using the recursive filter. The resulting interpolation errors are estimated here by approximating its effects as those of a Gaussian filter applied to the retrieved values. We use the same datasets and methodology as what was used for the estimation of the errors introduced resulting from the mismatch of the (Gaussian) sensor and desired (boxcar) averaging patterns.

For the layer-averaged water vapor mixing ratios ( $r(\text{mid})$ ,  $r(\text{high})$ ,  $r(\text{low})$ ) retrieved at high resolution (15 km), the interpolation errors as simulated here by the smoothing of the sensor-averaged fields are of the same order as those introduced by the sensor averaging pattern, leading to aggregate rms errors about twice as large as those resulting from the sensor averaging alone. Time-averaged relative rms aggregate errors are less than 5% for any of the cases for  $r(\text{high})$ , less than 3% for  $r(\text{mid})$ , and less than 2% for  $r(\text{low})$ .

## 10. Appendix D — Estimate of Cell Mismatch Errors

### 10.1. Introduction

The goal of this study was to quantify the difference between two horizontal averaging methods when these are applied to typical geophysical fields of CMIS EDRs: layer temperature and water vapor mixing ratio and total water substance; and of vertically integrated water vapor, liquid and ice. The EDRs are required by the SRD to be validated against averages over square areas of size 15-50 km on a side, depending on the EDR. The actual retrieved quantities have spatial properties defined by the CMIS sensor and the Footprint Matching algorithm and are approximately Gaussian averages where the width at half-height of the Gaussian filter is equal to the length of the side of the square verification cell. Here we examine the differences obtained by applying two convolution filters to high resolution model simulations. The square unit and truncated Gaussian response convolution filters are described in section 10.2. The high resolution model simulations are from University of Wisconsin case studies of extreme events on a 2.5 or 2.34 km grid. These are described in section 10.3. The definition of the statistics calculated is given in section 10.4. Typical examples are given in section 10.5. We then present a summary of the statistics of the differences which we calculated (section 10.6), and a discussion of how to apply the results (section 10.7). The final section (10.8) is an analysis of the cell mismatch errors for sea surface temperature, which was performed with a different dataset.

When the results obtained here are applied, the differences between the two filters are interpreted as errors due to the sampling pattern of the sensor composites. To the extent that the forward problem and retrieval process are linear, the retrieved environmental quantities are also approximately equal to the same Gaussian filter applied to the true environmental quantities. Any non-linear behavior is evaluated separately for the EDRs in their respective ATBD volumes.

### 10.2. Convolution filters

We define two convolution filters—the square unit response filter (SURF) and the truncated quasi-Gaussian filter (TQGF). Both are implemented as a weighted sum over a square of grid points.

$$f(x)_{rs} = \sum_{j=-n}^n \sum_{i=-n}^n w_{ij} x_{r+i, s+j}$$

Here  $n$  is number of grid points that the filter extends in each direction from the central point. Thus the dimension of the stencil is  $(2n+1)$  by  $(2n+1)$ . The weights are normalized so that the sum of all the weights is one. More exact methods of integration are not necessary for this study.

For the SURF, the weights before normalization are all taken to be one, except for the grid points at the edges, for which the weights are taken to be the fraction of the grid cell covered by the square. For the TQGF with a width at half height of  $h$ , the length parameter for the Gaussian function is

$$s = \frac{h}{2\sqrt{\ln(2)}}$$

and the weights before normalization are given by,



$$w_{ij} = \exp \frac{-\delta^2 [i^2 + j^2]}{s^2}$$

Here delta is the grid increment. The Gaussian function must be truncated at some point and we use 3.5 times the halfwidth as the total stencil width which is equivalent to truncating the filter at 3s (since s is  $\sqrt{2}$  times the “standard deviation” of the Gaussian function, this corresponds to ~4.5 standard deviations). The values of h and the values of n for the 2.34 and 2.5 km grids are:

Variable	AVTP	AVMP	ITWC	PW	LWP	IWP	RR
h (km)	40	15	20	25	20	50	15
n (2.34 km)	30	12	15	19	15	38	12
n (2.5 km)	28	11	14	18	14	35	11

Here AVTP is the temperature profile, AVMP is the moisture profile, and (ITWC, PW, LWP, IWP) are integrated water (total, vapor, liquid, ice) respectively, and RR is rain rate. The LWP (liquid water path) and IWP (ice water path) is applicable to our interpretations of the CLW and CIWP EDRs, respectively. Note that RR was available only for the Friuli model run.

In what follows we define error as the difference between truth and observed, or between SURF and TQGF. The difference between the two filters is illustrated in Figure D.1 which shows the weights for the SURF and TQGF in black and their difference in red for halfwidths of 15, 25, and 50 km. For plotting purposes all the weights are normalized by the maximum weight of the SURF. The difference may also be considered a filter. Note that the maximum difference filter weight is half that of the other filters. Features with a scale equal to h/2 or with a wavelength equal to h will be picked up by the difference filter.

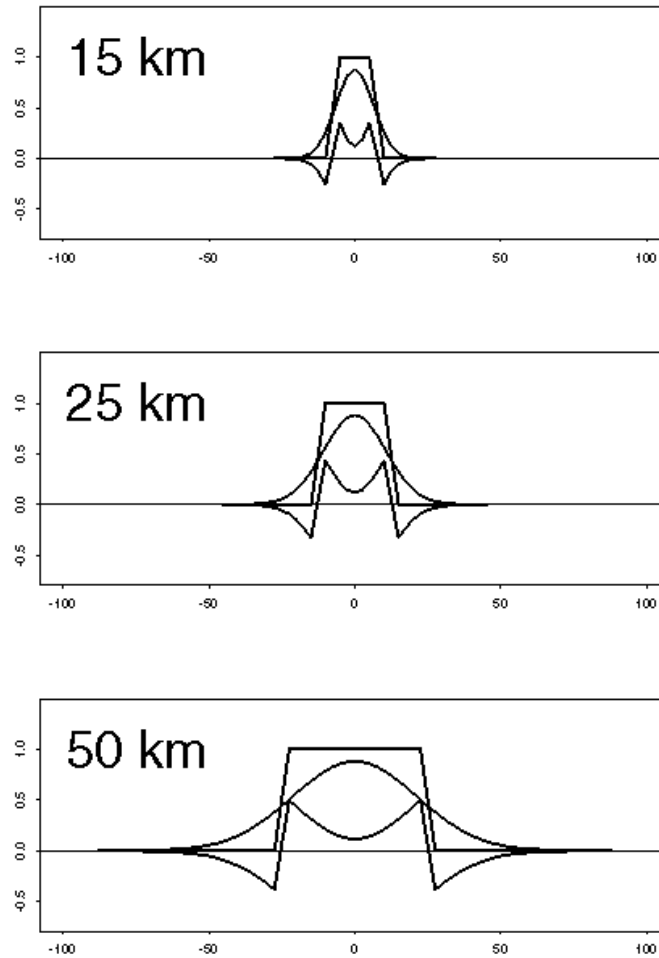


Figure D.1: The filter weights for the SURF and TQGF are plotted versus distance (km) from the center point of the filter stencil. All weights have been normalized so that the top of the SURF boxcar is at one. The difference (SURF-TQGF) is plotted in red. Results are shown for  $h = 15, 25$  and  $50$  km, and for  $\delta = 2.5$  km.

### 10.3. High resolution model simulations and preprocessing

The truth data were taken from the innermost grid of very high resolution mesoscale model forecasts created using the University of Wisconsin model (see acknowledgments below). This model is derived in part from the CSU RAMS model as described by Tripoli (1992a, 1992b). The data are on a regular (x,y,z) grid, with horizontal grid spacing  $\delta$ , and with vertical spacing of 200-1000 m. The innermost grid may move during the forecast period.

Units for the model variables are SI—temperatures in K, mixing ratios in kg/kg, integrated water quantities in  $\text{kg/m}^2$ . However for convenience we report horizontal distances in km. Layer quantities (AVTP, AVMP) are averaged with respect to z for three layers in the troposphere (low, mid, high) according to:

Variable	AVTP (low)	AVTP (mid)	AVTP (high)	AVMP (low)	AVMP (mid)	AVMP (high)
Bottom (km)	1	5	9	1	4	8
Top (km)	2	6	10	3	6	10

Note that the layers for AVTP are 1 km thick and for AVMP 2 km thick. AVTP(low) and AVMP(low) are calculated whenever allowed and set to missing where the topography (topo) is high. The model includes very complete cloud and precipitation physics, and accounts for several categories of hydrometeors. We sum cloud and rain mixing ratios to obtain the total water liquid mixing ratio, and we sum all categories of frozen hydrometeors (graupel, pristine, snow, aggregate) to obtain the total water ice mixing ratio. Water phase (vapor, liquid, ice) mixing ratios multiplied by air density  $\rho$  ( $\text{kg/m}^3$ ) are integrated from the surface to the highest model level to produce (PW, LWP, IWP). In addition the sum of water vapor, liquid, and ice (total water content) mixing ratios multiplied by air density  $\rho$  ( $\text{kg/m}^3$ ) is integrated for three layers in the troposphere (low, mid, high) according to:

Variable	ITWC(low)	ITWC(mid)	ITWC(high)
Bottom (km)	1	4	7
Top (km)	4	7	10

Note that the layers for ITWC are 3 km thick. ITWC(low) is calculated whenever allowed and set to missing where the topography (topo) is high. When needed T,  $\log(\rho)$  and  $\log(\text{mixing ratios})$  are interpolated linearly in z.

There are three cases, hereafter denoted bonnie, genoa, and friuli. The genoa and friuli cases are described by Tripoli et al. (2000). The bonnie case is described by Panegrossi et al. (2001). Details for these cases are as follows:

- bonnie:

The Hurricane Bonnie forecast was made from initial conditions at 0000 UTC 26 August 1998. Data are used at 36, 38, 40, 42 and 44 forecast hours, valid at times ranging from 1200 to 2200 UTC 27 August. (The initial conditions for this forecast are from a lower resolution run that started at 0000 UTC 25 August 1998.) The horizontal resolution of the data is 2.5 km on the 200 by 200 innermost grid, and the 39 vertical levels are:

0, 200, 400, 600, 800, 1000, 1220, 1462, 1728, 2021, 2343, 2697, 3087, 3516, 3987, 4506, 5077, 5705, 6395, 7145, 7895, 8645, 9395, 10145, 10895, 11645, 12395, 13145, 13895, 14645, 15395, 16145, 16895, 17645, 18395, 19145, 19895, 20645, 21395 m.

The corresponding level increments are 200 m thru 1000 m, then increasing smoothly to 750 m from 7000 m onward.

- genoa:

The Genoa flood forecast was made from initial conditions at 1200 UTC 26 September 1996. Data are used at 14, 20, 26, 32, 36 forecast hours, valid at times ranging from 0200 UTC 27 September to 0000 UTC 28 September. The horizontal resolution of the data is 2.34 km on the 180 by 180 innermost grid, and the vertical levels are equal to the first 37 levels of the Hurricane Bonnie case.

- friuli:

The Friuli flood forecast was made from initial conditions at 0000 UTC 5 October 1996[?]. Data are used at 42, 48, 54, 60 forecast hours, valid at times ranging from 1800 UTC 6 October to 1200 UTC 7 October. The horizontal resolution of the data is 2.34 km on the 200 by 160 innermost grid, and the vertical levels are equal to the first 37 levels of the Hurricane Bonnie case. (The innermost grid was added at hour 39, at 1500 UTC 6 October.)

In each case we applied our analysis only to times well into the model run, after the moist physics was thoroughly spun-up.

As an example of the detailed water substance simulation, Figure D.2, Figure D.3, and Figure D.4 show the distribution of the PW, LWP, and IWP in Hurricane Bonnie simulation at forecast hour 36. In the figures the heavy dark line is the land sea boundary. In these figures the upper left corner is North Carolina. For reference Wilmington, NC is located at 34:14N, 77:57W. [Degree:Minute notation used.] Small-scale waves in the PW field are associated with peaks in the LWP and IWP fields, all evidence of very intense cumulus convection. The basic statistics for these three fields are:

	N	mean	sd	rms	min	max
PW	40000	71.0	10.0	71.7	43.2	99.3
LWP	40000	1.77	3.70	4.11	0.00	47.1
IWP	40000	3.04	2.93	4.23	0.00	22.4

Here the column headings indicate the sample size, the mean, the standard deviation, the root mean square, the minimum, and the maximum. Note the very large maximum values in all three fields. These cases represent the upper limit of moist environments and are highly stressing relative to global average conditions.

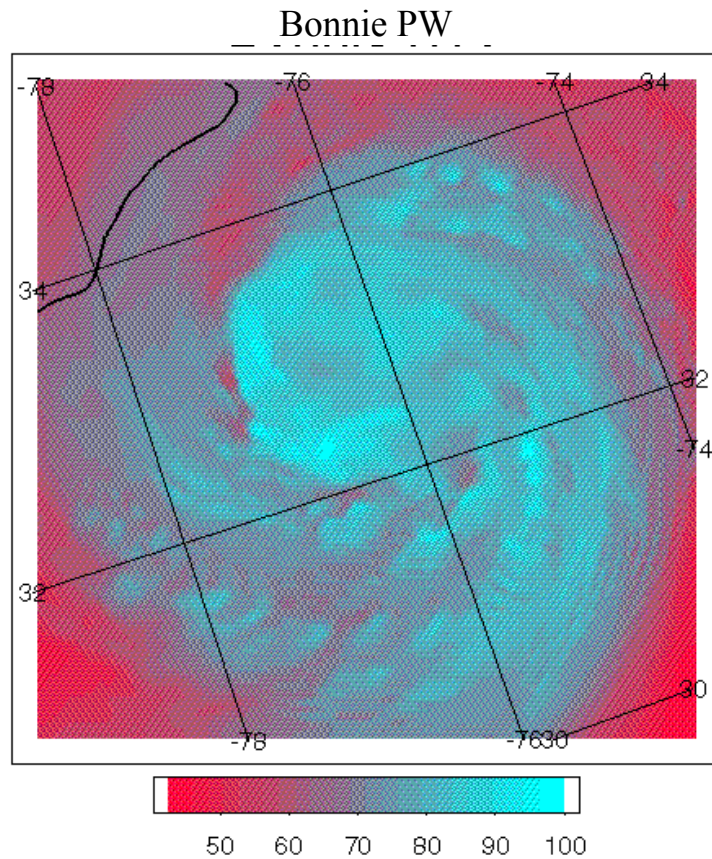


Figure D.2: PW image ( $\text{kg/m}^2$ ) for the Hurricane Bonnie simulation at hour 36. Here and in the images to follow, approximate latitude and longitude lines are overplotted in green, and the scale for the image is shown on the color bar below the image.

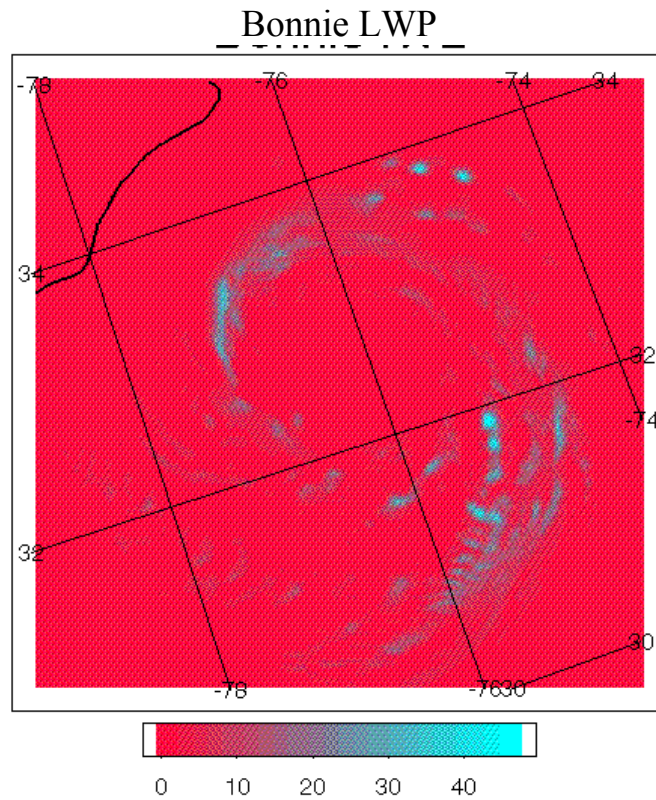


Figure D.3: LWP image ( $\text{kg}/\text{m}^2$ ) for the Hurricane Bonnie simulation at hour 36.

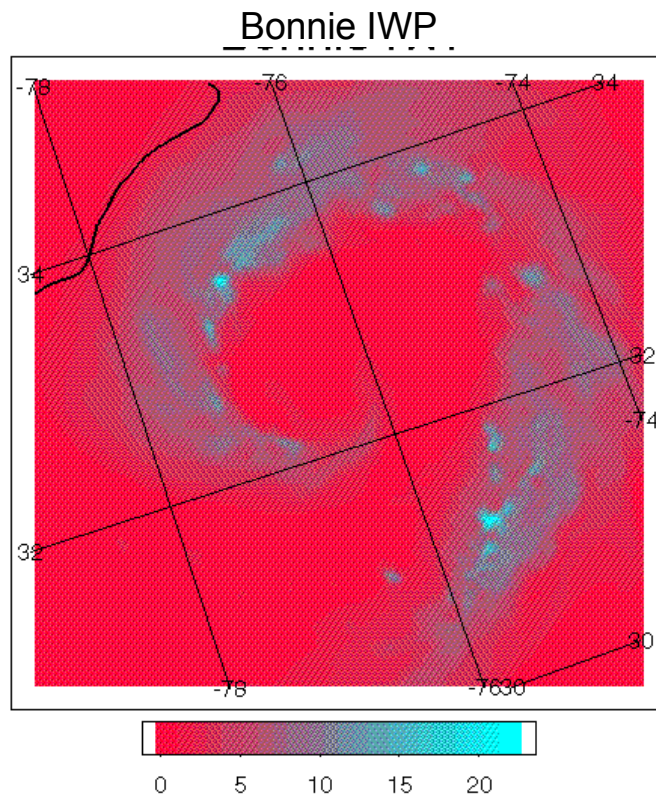


Figure D.4: IWP image ( $\text{kg}/\text{m}^2$ ) for the Hurricane Bonnie simulation at hour 36.

#### 10.4. Definition of statistics

For any field  $z$ , we calculate the SURF field  $z_s$  and the TQGF field  $z_g$ , every  $5 \delta$  (roughly every 12 km). The absolute error (AE) of  $z$  is

$$z_{ae} = z_s - z_g$$

and the relative error (RE) of  $z$  is defined here as

$$z_{re} = \frac{(z_s - z_g)}{\max(z_s, z_g)}$$

For any error  $e$  we calculate the mean and rms of  $e$  as  $\langle e \rangle$  and  $\sqrt{\langle e^2 \rangle}$  where  $\langle \rangle$  indicates an average over the sample of non-missing values. In addition we report the number of non-missing values  $N$ . Note that the larger the value of  $h$ , the larger the filter stencil and larger the boundary between the grid domain edge and the first filtered value.

In what follows the standard error calculations are denoted by the letter E. Error calculations for  $h=15$  for  $r$  layer quantities are denoted by the letter H.

Because the cases studied have such extreme values of integrated water quantities we have repeated our calculations for these quantities after editing these fields by replacing values in excess of a critical value by that critical value. Error calculations allowing no precipitation and light precipitation only, for (PW, LWP, IWP, RR) are denoted by the letters N and L, respectively, and correspond to critical values as given here:

variable	L-critical-value	N-critical-value
PW (kg/m <sup>2</sup> )	75.0	75.0
LWP (kg/m <sup>2</sup> )	5.0	0.5
IWP (kg/m <sup>2</sup> )	2.6	0.3
RR (mm/hr)	50.0	NA

The L critical values are equal to the high end of the SRD measurement range and the N critical values are equal to precipitation thresholds. The editing of the L and especially the N fields can create plateaus in the edited fields which results in vanishingly small errors. Therefore we calculated the L and N statistics again masking out grid points where  $z_s > 0.999 z_{crit}$ . These statistics are denoted by the letters M and O.

#### 10.5. Example calculations

As examples we show these calculations for the Fiuli case at forecast hour 54 for AVTP(mid) and PW. Figure D.5 described the lower boundary topography, which reaches 3000 m. This topography is inversely correlated with the PW. Mountains in the upper right corner are the Dolomites, and mountains along the left side are the Apennines. For reference Venice is located at 45:27N, 12:21E, near the center of the plot. Figure D.6 shows the mid level temperature field at full resolution. Figure D.7 and Figure D.8 show the result of applying the SURF and TQGF to this field. Note that the stencil for the SURF is much smaller than for the TQGF, so a larger part of the domain is filtered. Note also the change in scales for temperature. The overall features are retained, but some smoothing is apparent for both filters. The TQGF provides somewhat

more smoothing than the SURF. Figure D.9 shows the AE for this field. The basic statistics for the fields shown in Figures D.6 through D.9 for this case are:

	N	mean	sd	rms	min	max
z	32000	263	1.8	263	258	270
z_s	1073	263	1.7	263	259	267
z_t	560	263	1.2	263	259	265
100*z <sub>ae</sub>	560	-0.4	6.6	6.7	-23	16

Similar figures show the PW field for this case and time. Figure D.10 shows the PW field at full resolution. Figure D.11 and Figure D.12 show the result of applying the SURF and TQGF to this field. Figure D.13 and Figure D.14 show the AE and RE for this field. The patterns of AE and RE are very similar in this case. This does not hold for LWP and IWP where in areas of the original field which are zero the values of AE are small, but the values of RE are large and negative. The basic statistics for the fields shown in Figures D.10 through D.14 for this case are:

	N	mean	sd	rms	min	max
z	32000	29.24	7.10	30.09	10.28	43.03
z_s	1140	29.42	6.94	30.22	13.56	42.37
z_g	825	30.56	6.43	31.23	14.70	42.15
100*z <sub>ae</sub>	825	-0.04	34.90	34.91	-184.85	121.97
100*z <sub>ae</sub>	825	-0.15	1.36	1.37	-7.04	3.06



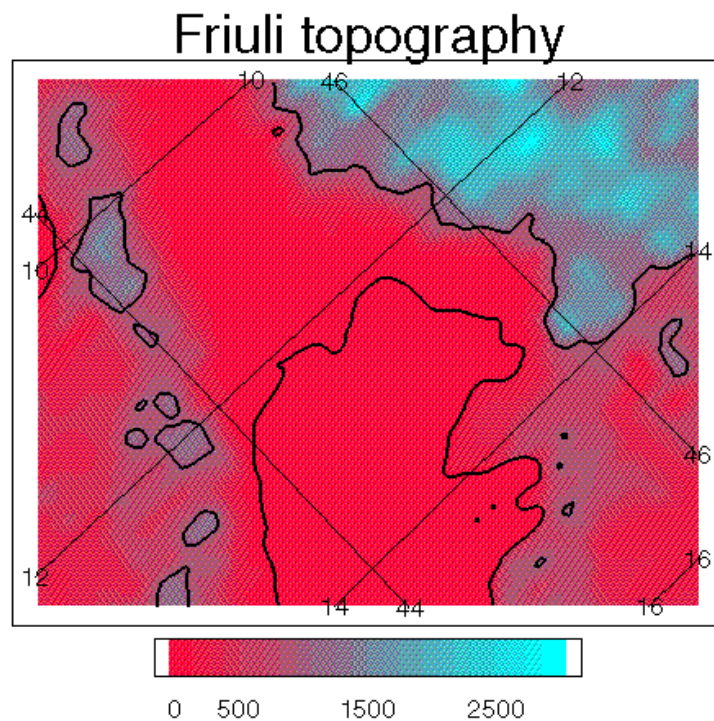


Figure D.5: Friuli base map showing the model topography (m). Contours are added for the land sea boundary (black) and the 1000 m height level (green).

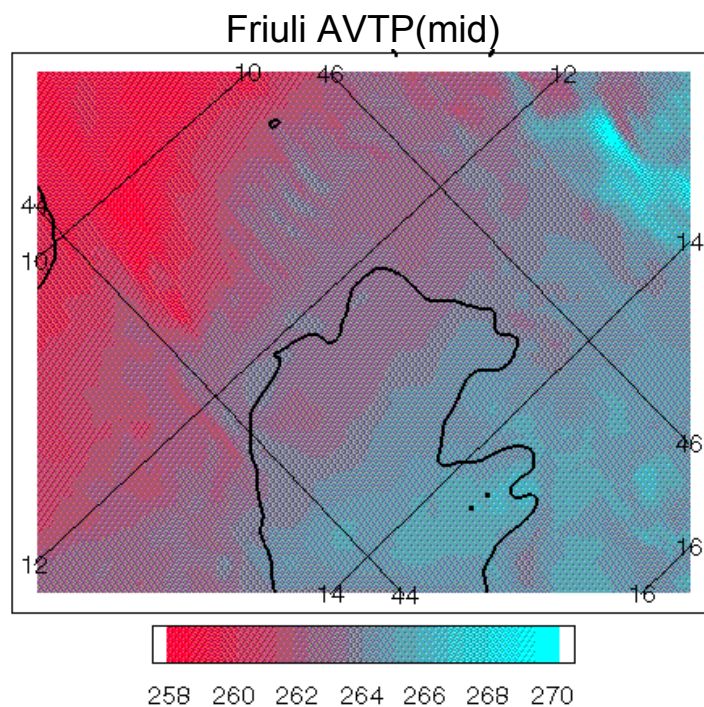


Figure D.6: The mid level temperature field (K) for the Friuli case at forecast hour 54.

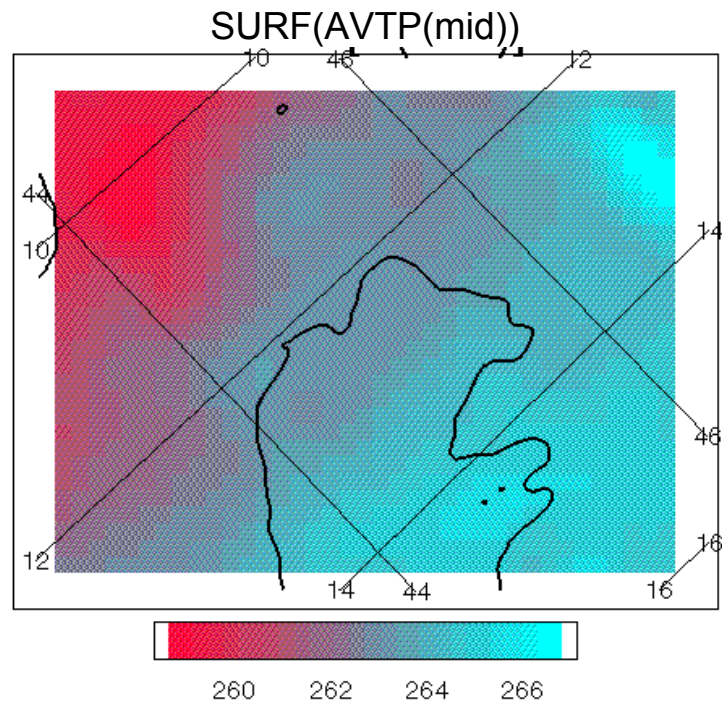


Figure D.7: The mid level temperature field (K) for the Friuli case at forecast hour 54, filtered with the SURF.

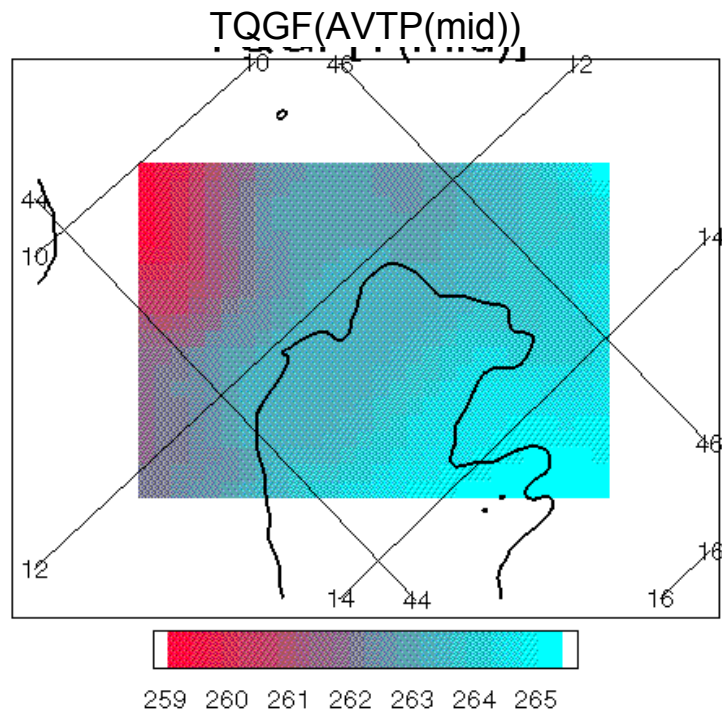


Figure D.8: The mid level temperature field (K) for the Friuli case at forecast hour 54, filtered with the TQGF.

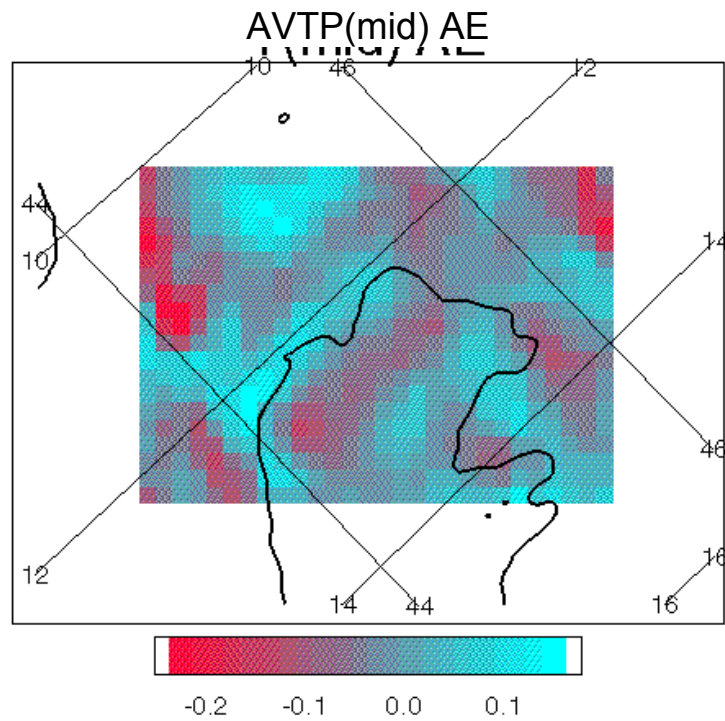


Figure D.9: The mid level temperature field AE (K) for the Friuli case at forecast hour 54.

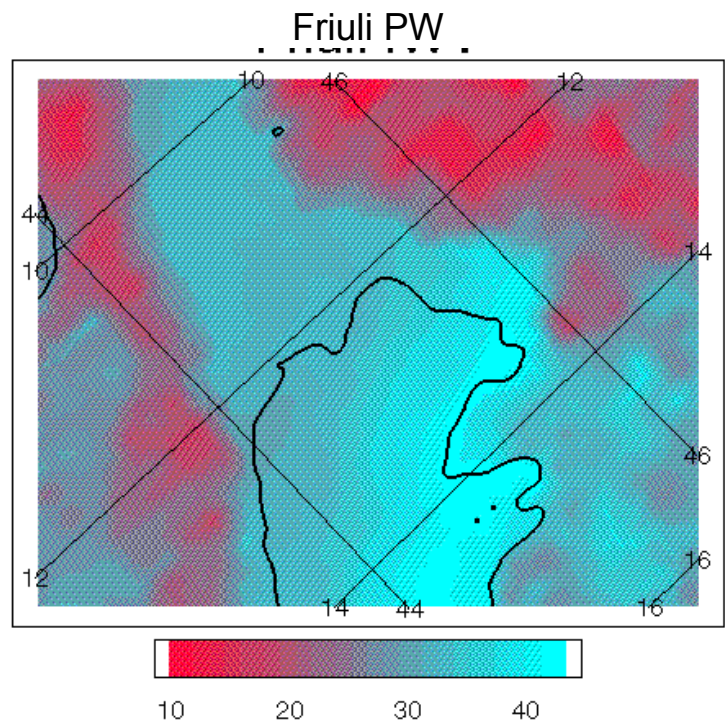


Figure D.10: The PW field (kg/m<sup>2</sup>) for the Friuli case at forecast hour 54.



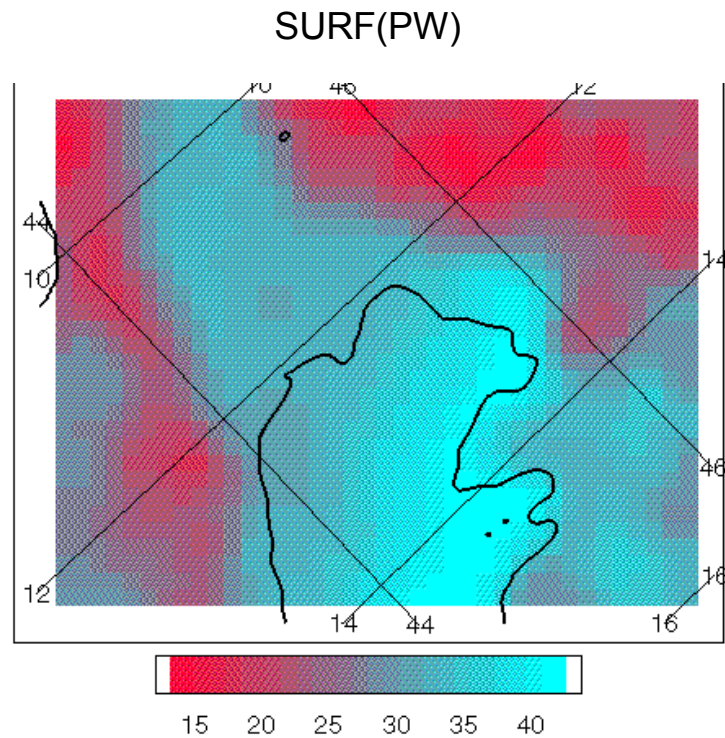


Figure D.11: The PW field ( $\text{kg/m}^2$ ) for the Friuli case at forecast hour 54, filtered with the SURF.

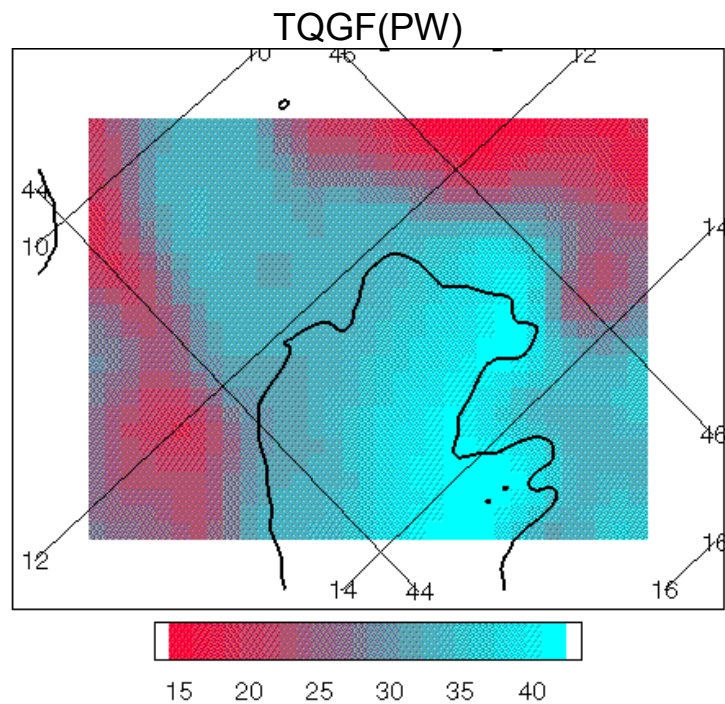


Figure D.12: The PW field ( $\text{kg/m}^2$ ) for the Friuli case at forecast hour 54, filtered with the TQGF.

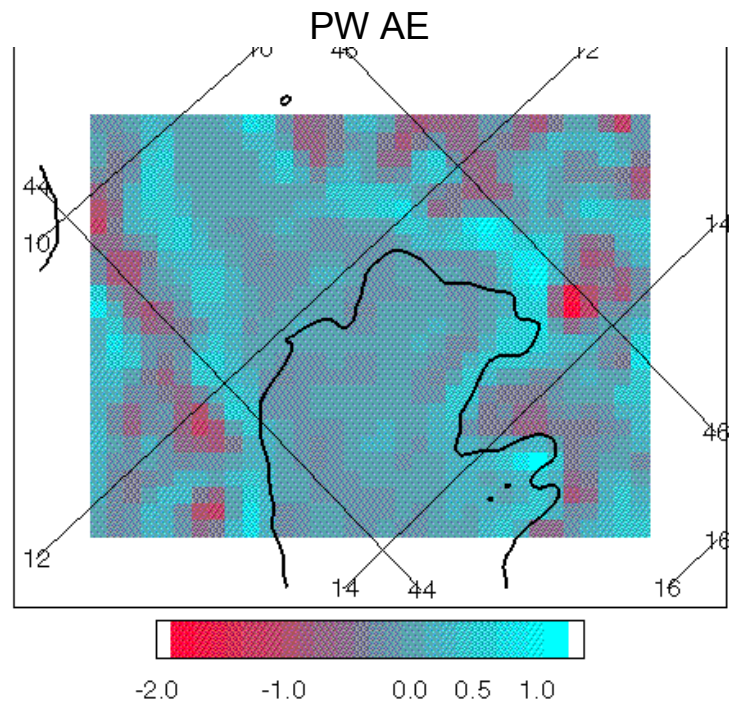


Figure D.13: The PW field ( $\text{kg/m}^2$ ) AE for the Friuli case at forecast hour 54.

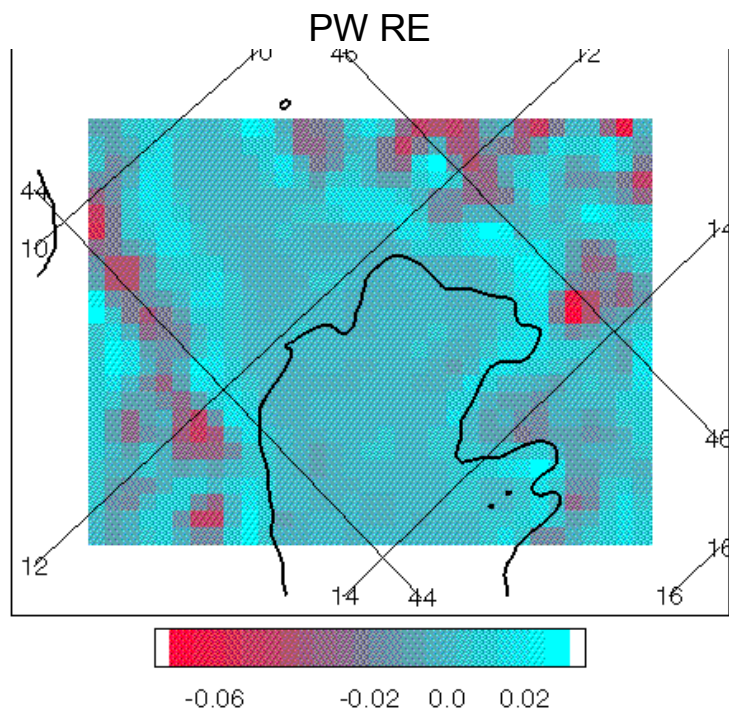


Figure D.14: The PW field ( $\text{kg/m}^2$ ) RE for the Friuli case at forecast hour 54.

## 10.6. Results

### 10.6.1. All variables

Here we report the RMS AE and RMS RE (as a percentage) for each case, averaged over all available times. In addition to all the ‘E’ (standard) and ‘H’ (high resolution) error statistics we include the ‘L’ (light precip) and ‘N’ (no precip) error statistics for LWP and IWP. Further we report the ratio of the standard deviations of the AE to the SURF fields as a percentage.

var	RMS AE		
	friuli	genoa	bonnie
E.AVTP(low)	7.85 e-02	7.30 e-02	1.21 e-01
E.AVTP(mid)	5.84 e-02	8.88 e-02	1.10 e-01
E.AVTP(high)	3.94 e-02	7.35 e-02	1.08 e-01
E.AVMP(low)	4.91 e-05	8.47 e-05	1.99 e-04
E.AVMP(mid)	3.54 e-05	5.61 e-05	1.86 e-04
E.AVMP(high)	9.20 e-06	1.53 e-05	9.41 e-05
H.AVMP(low)	2.78 e-05	4.41 e-05	1.13 e-04
H.AVMP(mid)	1.71 e-05	4.25 e-05	8.14 e-05
H.AVMP(high)	4.67 e-06	8.92 e-06	3.91 e-05
E.ITWC(low)	4.20 e-05	9.35 e-05	1.64 e-04
E.ITWC(mid)	2.85 e-05	1.25 e-04	1.42 e-04
E.ITWC(high)	2.11 e-05	1.03 e-04	8.62 e-05
E.PW	3.43 e-01	4.25 e-01	5.16 e-01
E.RR	4.98 e-01	NA	NA
E.LWP	8.09 e-02	2.53 e-01	3.92 e-01
L.LWP	7.04 e-02	1.05 e-01	1.64 e-01
N.LWP	1.54 e-02	1.65 e-02	1.81 e-02
E.IWP	9.74 e-02	4.83 e-01	2.96 e-01
L.IWP	6.55 e-02	8.42 e-02	1.20 e-01
N.IWP	1.19 e-02	1.17 e-02	1.07 e-02

var	100*RMS RE		
	friuli	genoa	bonnie
E.AVTP(low)	0.03	0.03	0.04
E.AVTP(mid)	0.02	0.03	0.04
E.AVTP(high)	0.02	0.03	0.04
E.AVMP(low)	0.67	0.82	1.41
E.AVMP(mid)	1.99	1.78	2.64
E.AVMP(high)	3.72	4.34	5.28
H.AVMP(low)	0.39	0.51	0.89
H.AVMP(mid)	0.81	1.29	1.23
H.AVMP(high)	1.47	2.33	2.47
E.ITWC(low)	0.58	0.90	1.25
E.ITWC(mid)	1.11	2.63	1.91
E.ITWC(high)	2.15	5.08	2.72
E.PW	1.35	1.47	0.71
E.RR	58.60	NA	NA
E.LWP	37.90	46.13	25.00

L.LWP	37.86	45.72	23.09
N.LWP	36.97	43.22	17.49
E.IWP	21.71	34.92	21.91
L.IWP	21.26	30.34	18.46
N.IWP	20.06	26.26	9.20

var	100*Mean[sd(z <sub>ae</sub> )/sd(z <sub>s</sub> )]		
	friuli	genoa	bonnie
E.AVTP(low)	5.95	4.89	12.61
E.AVTP(mid)	5.23	11.38	7.78
E.AVTP(high)	3.96	10.44	5.82
E.AVMP(low)	6.32	2.20	9.99
E.AVMP(mid)	5.55	11.89	8.50
E.AVMP(high)	8.48	14.88	12.57
H.AVMP(low)	3.26	3.18	4.93
H.AVMP(mid)	2.49	7.87	3.50
H.AVMP(high)	4.01	8.44	4.61
E.ITWC(low)	4.48	6.91	6.45
E.ITWC(mid)	3.88	13.85	5.61
E.ITWC(high)	5.46	14.89	5.99
E.PW	4.52	4.10	4.58
E.RR	11.97	NA	NA
E.LWP	12.05	19.70	15.55
L.LWP	11.32	17.14	12.27
N.LWP	9.13	13.65	9.77
E.IWP	11.47	22.84	16.30
L.IWP	10.24	12.35	14.03
N.IWP	13.82	10.56	17.18

The RMS RE and AE vary with forecast time within each case. The values for each forecast time are within a factor of two of the overall value reported in the above tables.

In these tables we do not show the M and O statistics. Calculations for M are the same as L and for O are the same as N except that the plateaus are masked. Generally masking the plateaus tends to increase the rms AE by less than 5% for friuli and genoa. For bonnie, the fraction of the domain which is masked is 30-40% for PW and often more than 40% for IWP. In these cases, the PW rms AE increase by 30%, and some of the no rain IWP rms AE increase by 50%. In addition, there is one very exceptional case: For bonnie, at 2880, there is a very substantial cirrus shield around the center of the storm, and the O rms AE (0.0164 kg/m<sup>2</sup>) is nearly twice the N rms AE (0.0086 kg/m<sup>2</sup>). However even for bonnie the overall RMS AE is not much effected by masking of the plateaus.

var	AE for bonnie				
	E	L	M	N	O
LWP	0.3924	0.1643	0.1646	0.0181	0.0194
IWP	0.2957	0.1203	0.1243	0.0107	0.0141

The effect of masking the plateaus on the RE is also small, and described further in the next subsection.

### 10.6.2. Further RE statistics using masking for the hydrometeors.

The RE for LWP, IWP, and RR are very high. There are three factors responsible. First, precipitation occurs on scales similar in size to the scales of the difference filter (i.e. on scales equal to half the halfwidth.) Second, the cases studied are extreme. Third, the RE calculation is heavily influenced by areas of essentially zero hydrometeors. We can account for this third effect by masking out small values in the calculation of RE statistics.

The relative error calculations for LWP and IWP are dominated by regions of zero precipitation because the stencil for the TQGF is so much larger than for the SURF. The actual composite footprint patterns tend to taper off more quickly than the Gaussian. When the model hydrometeor mixing ratios are zero, the absolute errors approach zero, but the relative errors approach -1.0. Therefore we calculated the LWP and IWP statistics again masking out grid points where  $z_s < z_{eps}$ , where  $z_{eps}$  may be (0.5, 0.25, 0.01) for LWP, (0.2, 0.1, 0.01) for IWP, and (5, 1, 0.01) for RR. These statistics are denoted ('E','L','M','N','O') followed by ('a','b','c') which correspond to the three levels indicated. We use 'O' to indicate the statistics obtained without masking of low values (as in Section 10.6.1).

Masking the low values greatly reduces the RMS values and the sample size and mean values of the relative errors. RMS unrestricted relative errors (E), accumulated over all forecast times, range from 20 to 50%. Errors restricted to light precip (Lc,Mc) and with  $z_{eps}=0.01$  (c) are typically 20%. This reduces to 15% with  $z_{eps}=(LWP=0.25, IWP=0.1, RR=1)$ . Errors restricted to no precip (Nb,Ob) and with  $z_{eps}=(LWP=0.25, IWP=0.1)$  are typically 6%.

Differences between Lx and Mx RMS relative errors over all times, and between Nx and Ox (i.e. masking the plateaus) are very small except for bonnie IWP, which itself is not large compared to the difference between cases.

Considering variations with forecast time (not shown), there are some general trends. As masking increases there is more variation of sample size, less variation of rms relative error, and the bias changes character from sensor > truth towards sensor < truth. While these trends are general and expected, they are more pronounced for LWP than for IWP, and for the Italian floods than from bonnie.

In these tables, N is the average sample size per time.



Relative error for LWP accumulated over all times													
	RMS				N				Mean				
	a	b	c	0	a	b	c	0	a	b	c	0	
friuli:	E	9.68	11.37	18.34	37.90	189	285	630	884	0.54	-1.47	-5.78	-19.49
	L	9.35	11.05	18.23	37.86	189	285	630	884	0.69	-1.33	-5.71	-19.44
	M	9.35	11.05	18.23	37.86	189	285	630	884	0.69	-1.33	-5.71	-19.44
	N	NA	5.19	15.63	36.97	0	275	630	884	NA	2.12	-3.28	-17.67
	O	NA	5.96	16.58	38.52	0	205	560	814	NA	2.59	-3.78	-19.25
genoa:	E	18.46	19.72	28.50	46.13	124	186	420	900	0.72	-1.88	-11.06	-26.76
	L	14.77	16.60	27.11	45.72	123	185	419	899	3.43	0.30	-9.91	-26.21
	M	14.78	16.61	27.11	45.73	123	185	419	899	3.43	0.29	-9.91	-26.22
	N	NA	8.12	19.45	43.22	0	142	420	900	NA	5.15	-4.70	-23.36
	O	NA	8.52	19.80	43.59	0	126	404	885	NA	5.51	-4.96	-23.80
bonnie:	E	16.02	18.08	21.89	25.00	636	780	1162	1225	-3.48	-5.70	-9.09	-10.98
	L	11.68	14.33	19.56	23.09	635	779	1162	1225	-0.92	-3.33	-7.36	-9.33
	M	11.76	14.40	19.63	23.17	627	771	1154	1217	-0.96	-3.38	-7.42	-9.41
	N	0.96	4.55	12.16	17.49	156	707	1162	1225	0.48	1.59	-2.62	-4.81
	O	NA	5.20	13.17	18.87	0	534	989	1052	NA	1.92	-3.17	-5.69

Relative error for IWP accumulated over all times													
	RMS				N					Mean			
	a	b	c	0		a	b	c	0	a	b	c	0
friuli:	E	10.84	12.19	16.16	21.71	279	336	402	425	-2.46	-4.12	-6.56	-9.39
	L	9.54	11.14	15.50	21.26	279	336	402	425	-1.77	-3.50	-6.04	-8.90
	M	9.54	11.14	15.51	21.26	279	336	401	425	-1.77	-3.51	-6.04	-8.91
	N	4.36	5.81	12.30	20.06	172	246	314	338	2.48	0.56	-2.91	-6.57
	O	4.51	5.97	12.57	20.48	158	232	301	324	2.57	0.51	-3.12	-6.91
genoa:	E	21.25	24.64	28.68	34.92	220	266	408	441	-6.43	-9.74	-14.38	-18.82
	L	12.89	16.29	22.30	30.34	213	260	403	436	-1.28	-4.30	-9.83	-14.66
	M	13.04	16.45	22.45	30.53	208	255	398	431	-1.35	-4.42	-9.98	-14.85
	N	5.35	7.14	14.14	26.26	91	170	334	367	4.22	2.33	-4.38	-10.34
	O	5.49	7.26	14.28	26.50	84	163	327	360	4.33	2.30	-4.53	-10.59
bonnie:	E	17.15	18.86	21.58	21.91	637	658	675	676	-5.77	-6.99	-8.50	-8.65
	L	12.90	14.92	18.08	18.46	637	658	675	676	-3.23	-4.45	-5.95	-6.10
	M	13.46	15.55	18.82	19.22	584	605	622	623	-3.66	-4.98	-6.59	-6.75
	N	2.71	4.17	8.56	9.20	589	651	675	676	1.06	0.13	-1.15	-1.30
	O	3.72	5.62	11.54	12.41	282	344	368	369	1.54	-0.29	-2.62	-2.88

Relative error for RR accumulated over all times														
friuli:	RMS					N				Mean				
	a	b	c	0		a	b	c	0	a	b	c	0	
	E	9.39	12.46	24.20	58.60	84	220	496	743	1.42	-1.96	-10.59	-38.25	
	L	8.80	12.32	24.15	58.59	84	220	496	743	1.68	-1.89	-10.56	-38.23	
	M	8.80	12.32	24.15	58.59	84	220	496	743	1.68	-1.89	-10.56	-38.23	

## 10.7. Discussion

The difference between the SURF and TQGF applied to fields of temperature and water vapor ( $\tau$ , PW) is generally small even for the cases studied of very intense storms. The difference of these filters applied to fields of hydrometeors is however very significant in cases such as these. Generally the RE for the hydrometeor fields under these stressful conditions is 20% or more if heavy precipitation is allowed.

The reason is clear: precipitation occurs on scales similar in size to the scales of the difference filter (i.e. on scales equal to half the halfwidth. In addition the RE calculation is heavily influenced by areas of essentially zero hydrometeors.

## 10.8. Evaluation for Sea Surface Temperature

Cell mismatch errors are a particularly important concern for the sea surface temperature (SST) EDR because that EDR is retrieved from CFOVs that are considerably longer in one dimension (about  $82 \times 50$  km) than the verification cell (50 km square).

Cell mismatch errors were estimated by analyzing operationally-produced Pathfinder SST composite fields produced by Jet Propulsion Laboratory. The fields are produced at about 10 km resolution, which makes them suitable for evaluating spatial averaging effects on scales near that of the SST required horizontal cell size (50 km). The fields are produced from AVHRR infrared imager data after screening for clouds. The cloud screening provides an advantage of these composite products in comparison to single scenes. It is apparent from the structure of the fields, however, that some cloudiness is missed in the screening and that the compositing introduces spatial structure that can affect the spatial averaging analyses. These effects would tend to increase the estimated cell mismatch errors from the true values. The compositing process can have the opposite effect also to the extent that some SST gradients may be smeared by averaging in the presence of short-term SST changes.

Plots of SST and the cell mismatch error are in Figure D.15. The differences were computed with an assumed CFOV slightly smaller than the current baseline. The difference statistics (Figure D.16) indicate a difference standard deviation of about 0.07 K.

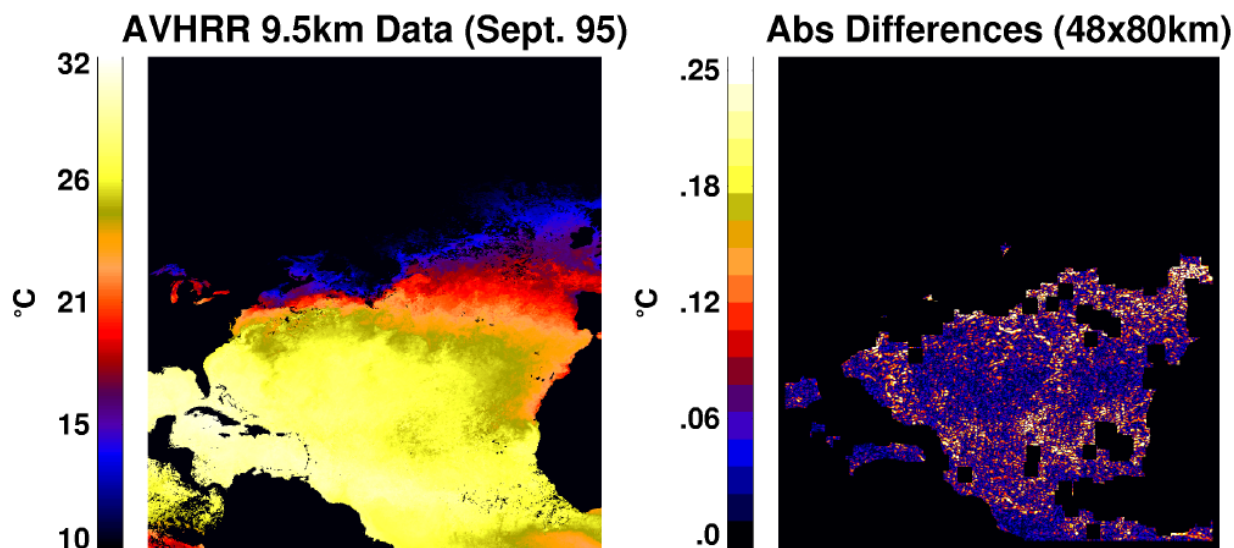


Figure D.15: SST field (left), with land areas blacked out, and the difference field between averaging over a 50-km square and a  $48 \times 80$ -km Gaussian ellipse (right). The blacked-out areas are more extensive in the difference field because we have excluded all areas where the averaging stencil encountered land.

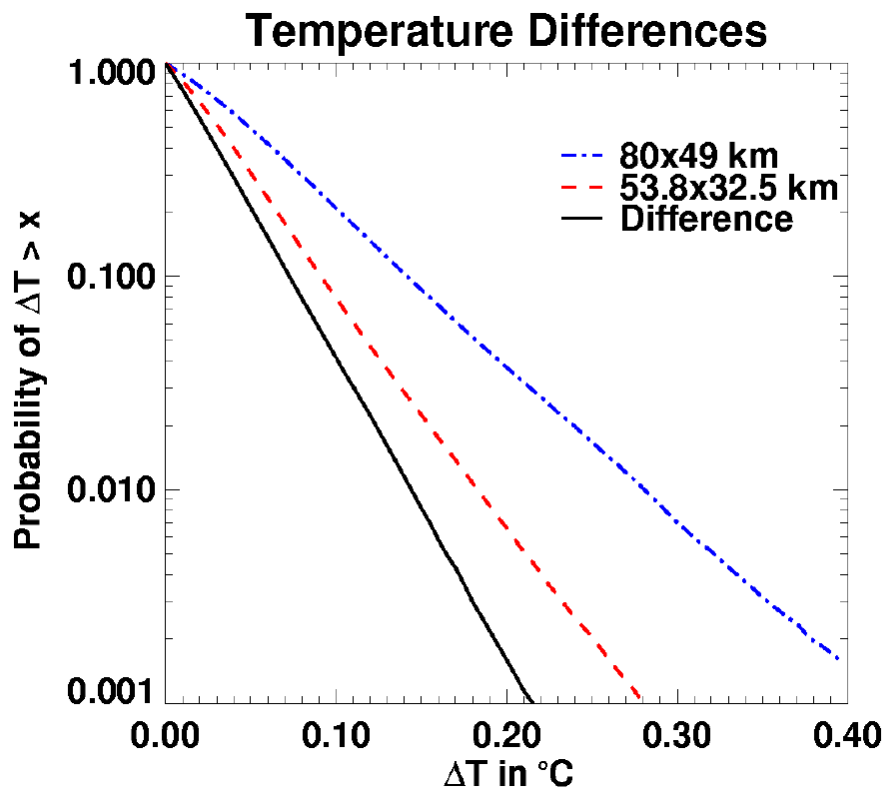


Figure D.16: Difference statistics for a 80×49-km elliptical Gaussian average and a 50-km square (dash-dot blue). The other curves may be disregarded. The statistics are plotted in terms of the probability of a difference greater than a given value.

### 10.9. Acknowledgments

The University of Wisconsin model data and advice on how to use these data were graciously provided by Gregory J. Tripoli and Giulia Panegrossi.